Tectonics®

RESEARCH ARTICLE
10.1029/2025TC008860

Key Points:

- Regional Sentinel-1 velocity maps (~130 m resolution) of the Tajik Basin and Dushanbe Trough reveal fault creep and slip partitioning
- The Ilyak Strike-slip Fault creeps to shallow depths at ~4–9 mm/yr, but deeper layers and other faults still pose an earthquake hazard
- Filtered velocity maps show widespread soil creep and active, slow-moving landslides, which could constitute a hazard

Supporting Information:

Supporting Information may be found in the online version of this article.

Correspondence to:

R. T. Walker, R. Wilkinson and S. Daout, richard.walker@earth.ox.ac.uk; rwilkinsonresearch@gmail.com; simon.daout@univ-lorraine.fr

Citation:

Wilkinson, R., Daout, S., Walker, R. T., Dodds, N., & Ischuk, A. (2025). Aseismic slip on the Ilyak Strike-slip fault (Tajikistan) and active fault and landslide hazards in and around the Tajik Basin revealed by InSAR. *Tectonics*, *44*, e2025TC008860. https://doi.org/10.1029/2025TC008860

Received 3 FEB 2025
Accepted 18 NOV 2025

Aseismic Slip on the Ilyak Strike-Slip Fault (Tajikistan) and Active Fault and Landslide Hazards in and Around the Tajik Basin Revealed by InSAR

R. Wilkinson[1], S. Daout[2], R. T. Walker[1], N. Dodds[1], and A. Ischuk[3]

[1]Department of Earth Sciences, COMET, University of Oxford, Oxford, UK, [2]Université de Lorraine, CNRS, CRPG, Nancy, France, [3]Institute of Geology, National Academy of Sciences, Dushanbe, Tajikistan

Abstract The Ilyak fault in Tajikistan is an E-W striking strike-slip fault, which forms the northern boundary of the actively deforming Tajik Basin fold and thrust belt. Determining the activity of the Ilyak fault is important for understanding the hazard to the nearby capital city of Dushanbe, and more generally in assessing the role of lithology in controlling fault behavior. Using a bespoke Multi-Temporal InSAR approach with ~5 years of Sentinel-1 satellite radar acquisitions, we produce regional surface velocity maps with a horizontal spatial resolution of ~130 m and numerical uncertainties below 1 mm/yr. Our rate maps reveal previously unrecognized details of creep, fault structure, and slip partitioning. We document creep on the Ilyak fault with a right-lateral rate of 8.1–8.7 mm/yr in the east reducing to 4.2–4.5 mm/yr in the west, as slip is progressively transferred to adjacent folds and thrusts in the Tajik Basin. Creep on the Ilyak fault and adjacent thrusts appears to be controlled by lithology, in particular the presence of evaporite-rich layers. Nonetheless, moderate earthquakes within the basement beneath the Ilyak fault, including a destructive M5.5 event in 1989, suggest potential earthquake hazards from deeper crustal layers. Using high-resolution Digital Elevation Models derived from optical stereo satellite data we document fault scarps north of the Ilyak fault, which may constitute an additional source of hazard. Filtered velocity maps also show evidence of soil creep and active, slow-moving landslides across the basin and in the mountains, constituting another hazard to local communities and infrastructure.

Plain Language Summary Tajikistan is prone to earthquakes and landsliding, both within the mountainous regions and in surrounding valleys, such as the wide basin in which the capital city of Dushanbe is situated. The major Ilyak active fault is mapped within this basin, and yet relatively few large earthquakes have been recorded in the area. We use satellite radar interferometry to image ground deformation in the region around Dushanbe. We show that the Ilyak fault is actually creeping at the surface, and so not storing up slip to be released in occasional earthquakes. This creep behavior is likely caused by the weak sedimentary rocks through which the fault runs. However, earthquakes that have occurred at depth beneath the creeping part of the fault and other potentially active faults in the vicinity both indicate ongoing earthquake hazard. Our surface rate maps also highlight widespread down-slope ground movement in slow landslides, offering a means of identifying and monitoring these hazards.

1. Introduction

The right-lateral Ilyak fault (IF) in Tajikistan is a major active strike-slip fault within the India-Eurasia collision (Figures 1 and 2a; Gągała et al., 2020; Metzger et al., 2020, 2021). It runs E-W along the northern margin of the Tajik Basin (also known as the Afghan-Tajik Depression), which contains a thick sedimentary sequence and is currently deforming on a series of prominent N-S to NE-SW trending thrust faults and folds. This fold and thrust belt is thought to result from stresses introduced by the adjacent Pamir plateau, which appears to be collapsing westward under gravity, with lowland shortening balanced by highland extension (Kufner et al., 2018; Schurr et al., 2014; Stübner et al., 2013). The IF accommodates right-lateral shearing along the northern edge of the fold and-thrust belt. It offers the potential to examine the mechanics of a major, rapidly slipping (Metzger et al., 2020, 2021), strike-slip fault which extends through a sequence of relatively weak sedimentary rocks (Gągała et al., 2020). Although the fault has hosted small to medium magnitude earthquakes up to M ~ 5.5 (M = magnitude; Djuraev & Shakirdzanova, 1993; Kufner et al., 2018), there is no record of larger events, suggesting that the IF may slip aseismically at least in some parts. The proximity of the IF to Dushanbe, the capital of Tajikistan (Figure 2a),

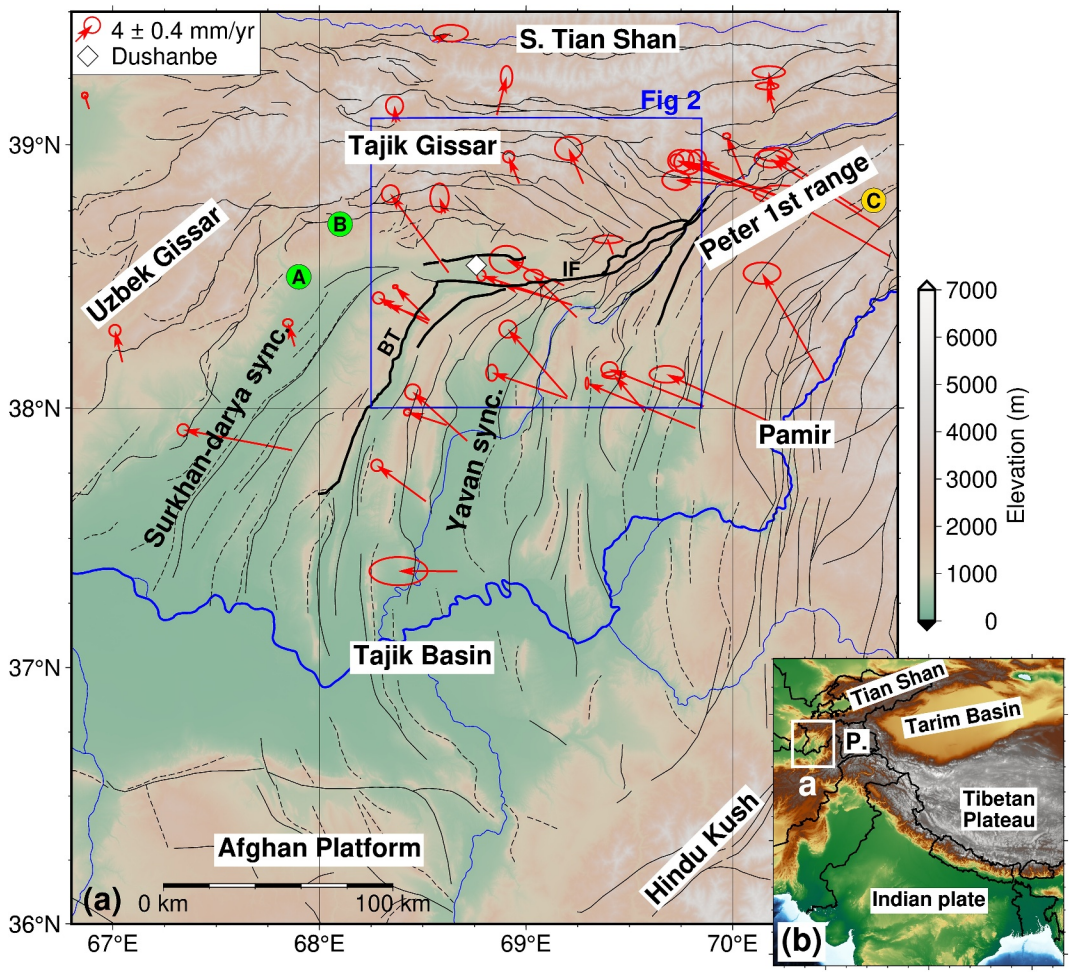

Figure 1. (a) The Tajik basin and surrounding regions. The Tajik Gissar is part of the southwestern part of the Tian Shan. Topography from 30 m SRTM DEM (Shuttle Radar Topography Mission (SRTM) Global, 2013) with major rivers in blue. Solid thin black lines are faults and dashed thin black lines are fold axes, both after Dedow et al. (2020) and Abdulhameed et al. (2020). Thick black lines highlight active faults discussed in this study. IF = Ilyak fault, BT = Bababtag thrust, sync = syncline. GNSS displacement rates (relative to stable Eurasia) from Metzger et al. (2020) and Zubovich et al. (2010) with 70% confidence ellipses. Blue box shows location of Figure 2. Circles A, B, and C show different proposed locations for the 1907 Karatag earthquake. Green circles A and B show the locations of two 1907 Karatag earthquake events (20 min apart) from Mikhailova et al. (2015). Yellow circle C shows the relocation of the Karatag earthquake proposed by Kulikova (2016), who found only one event. (b) Context map. P. = Pamir mountains. The white box shows the location of (a).

provides a separate compelling reason to examine the slip behaviour and earthquake potential of the IF, and of other nearby faults. Dushanbe has a reported population of around a million people (Statistical Agency under the President of the Republic of Tajikistan, 2022) and is particularly vulnerable to ground shaking due to its rapid expansion over the past few decades onto unconsolidated deposits and landslide-prone slopes (Pilz et al., 2013).

The interior of the Tajik Basin is characterized by a set of westward-convex folds and thrust sheets trending approximately N-S (e.g., Gągała et al., 2020; Kufner et al., 2018). In the northern part of the basin, most of the thrust sheets curve eastwards, having likely formed perpendicular to the IF and been dragged to an oblique angle over time due to the relative westwards motion of the basin. A notable exception is the westward-dipping Babatag thrust (BT) in the west of the basin, which meets the IF at right angles at around ~68.6°E (Figure 1). Large earthquakes in the region tend to be restricted to the surrounding mountains or their margins, such as the $M_W \sim 7.6$ 1949 Khait earthquake, which occurred on the boundary between the Pamir and the South Tian Shan, northeast of the region shown in Figure 1 (M_W = moment magnitude; Chen & Molnar, 1977; Evans et al., 2009; Bindi et al., 2014; International Seismological Centre, 2025). In 1907 the $M_W \sim 7.2$ Karatag (or Qaratog) thrust earthquake caused

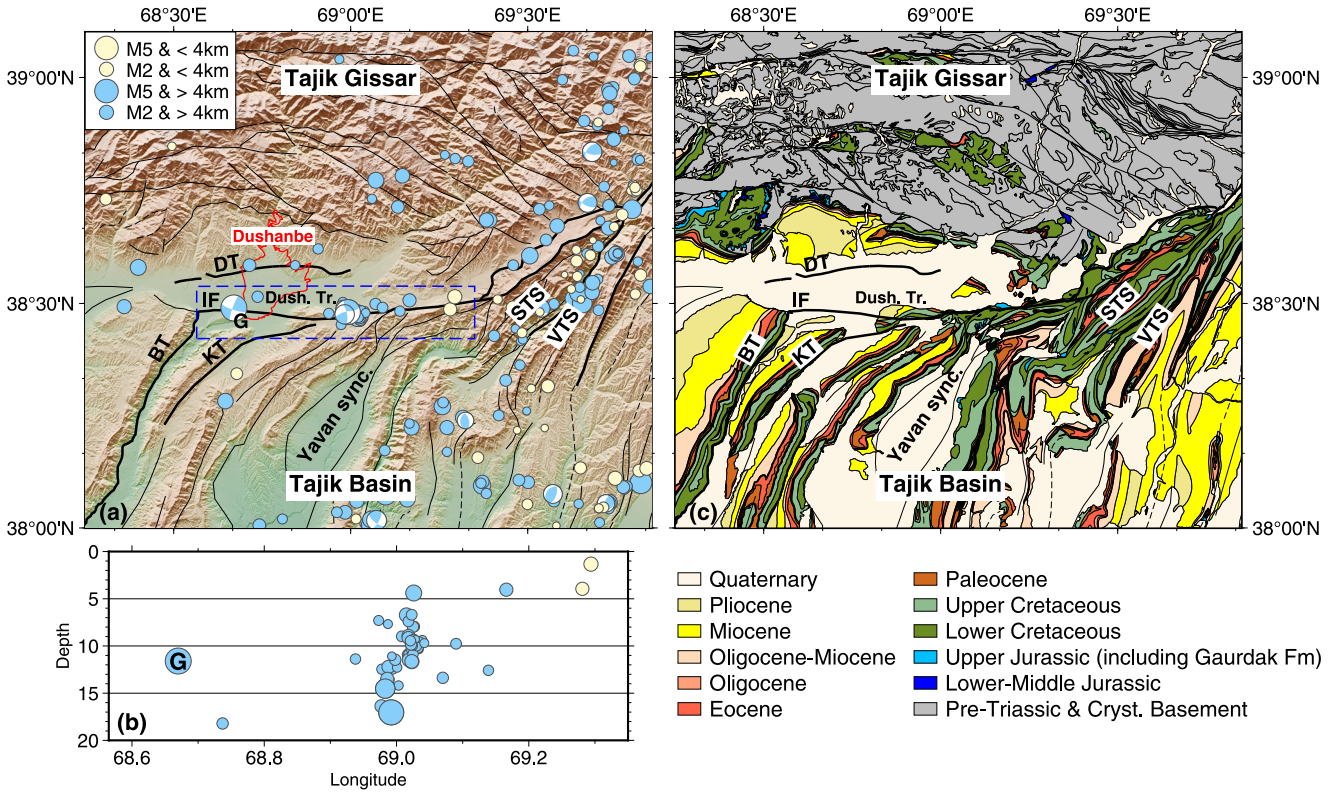

Figure 2. The northern Tajik basin, Dushanbe Trough (Dush Tr.) and southern Tajik Gissar. Solid thin black lines are faults and dashed thin black lines are fold axes, both after Dedow et al. (2020) and Abdulhameed et al. (2020). Thick black lines highlight active faults discussed in this study. IF = Ilyak fault, BT = Babatag thrust, DT = Dushanbe Trough thrust, STS = Surkhu thrust sheet, VTS = Vakhsh thrust sheet, sync = syncline. KT = Karchitau thrust (a) Topography from 30 m SRTM DEM. Earthquakes from 2008 to 2014 and focal mechanisms for larger events from Kufner et al. (2018), size relative to local magnitude. *G* = 1989 M5.5 Gissar earthquake (Djuraev & Shakirdzanova, 1993; International Seismological Centre, 2022; Storchak et al., 2020). Blue box shows region of earthquakes plotted in (b). Red polygon shows Dushanbe administrative boundary from OpenStreetMap contributors (2023). (b) Earthquakes in the vicinity of the Ilyak fault plotted by depth. (c) Geological map of the study region after Abdulhameed et al. (2020) and Gągała et al. (2020).

damage on the southern slopes of the Tajik Gissar (the southwestern part of the Tian Shan), with reports of more than 1500 fatalities (International Seismological Centre, 2025; Kalmetieva et al., 2009; Kondorskaya et al., 1982; Kulikova, 2016; Nikonov & Shebalina, 1979). There is, however, some disagreement in the published literature regarding the location of this event. Regional earthquake catalogues locate it on the southern edge of the Tajik Gissar (circles A and B in Figure 1), which is where the greatest macroseismic effects were reported (Kalmetieva et al., 2009; Kondorskaya et al., 1982; Mikhailova et al., 2015), implying rupture of the bounding thrust. Whereas, an international catalogue (International Seismological Centre, 2025) and an earthquake relocation using digitized seismograms (circle C in Figure 1; Kulikova, 2016) both report locations >200 km further east, within or close to the Peter the 1st range.

Previous geodetic studies in this region have documented the relative westward motion (with respect to stable Eurasia) of the Tajik basin, with notable deformation occurring on the IF and the BT (Ischuk et al., 2013; Metzger et al., 2020, 2021; Mohadjer et al., 2010; Zubovich et al., 2010). Using a small number of widely spaced GNSS (Global Navigation Satellite System) measurements, Metzger et al. (2020) estimated 8–15 mm/yr of strike-slip and ∼5 mm/yr of shortening across the IF, whilst a block modelling study based on regional GNSS velocities re-estimated the strike-slip rate to 11.5 ± 0.3 mm/yr and the shortening to 0.4 ± 0.5 mm/yr (Wang et al., 2024). Metzger et al. (2021) generated InSAR (Interferometric Synthetic Aperture Radar) rate maps with a horizontal resolution of ∼400 m covering the Tajik basin and the Pamir mountains region. Their findings reveal a strike-slip rate of around 10 mm/yr in the eastern part of the IF, decreasing to approximately 5 mm/yr in the west, as well as E-W convergence of ∼5 mm/yr on the BT. However, the Metzger et al. (2021) data set has limitations, being of low spatial resolution and strongly filtered, with a low signal-to-noise ratio and poor coverage in some areas. They

suggest the locking depth of the IF is ≤1 km, but cannot accurately constrain it further given the rate map resolution. Consequently, it is challenging to ascertain the extent to which the IF is slipping aseismically or accumulating strain. Additionally, the study does not address whether the observed velocity contrast around the IF zone is localized on a single structure or distributed across multiple faults.

Due to sparse GNSS observations, low-resolution and noisy InSAR maps, and a lack of detailed geomorphic mapping of active features, there is limited knowledge about the strain accumulation on individual active faults and folds in the Tajik Basin such as the IF. This lack of comprehensive data, combined with the multi-layered tectonics of the fold and thrust belt, makes it challenging to assess the seismic potential of this region accurately. To address this data gap, it is essential to conduct continuous high-resolution mapping of surface deformation rates across the basin.

In this study, we conducted a Multi-Temporal InSAR (MT-InSAR) analysis across the Tajik basin, by analysing networks of 451 (ascending track) and 588 (descending track) interferograms from ∼5 years of Sentinel-1 data to provide a continuous and high-resolution mapping of the deformation. Using a bespoke processing approach, we generated rate maps with high spatial resolution (∼130 m) and coverage, which are robustly constrained by redundant interferometric networks (Figure S1 in Supporting Information S1) and corrected with atmospheric delay models (Text S1.3 in Supporting Information S1). By adopting this processing method, we determine the extent of aseismic creep on the IF, and the slip partitioning between the IF and neighboring structures. Furthermore, we produce the first velocity map to capture ground deformation in the southern part of the Tajik Gissar mountains and across the thrust sheets in the northeast corner of the Tajik basin. By high-pass filtering the velocity maps, we identify and measure shorter wavelength surficial processes, such as slow-moving landslides. We also integrate InSAR measurements with geomorphic mapping, utilizing high-resolution Digital Elevation Models (DEMs) around Dushanbe for further identification and mapping of active faults. Finally, we discuss the implications of the results for seismic and landslide hazards in Dushanbe.

2. Seismo-Tectonic Setting

The Tajik basin is a fold and thrust belt in Central Asia, bounded by the Afghan platform to the south, the Tajik Gissar mountains to the north, the Uzbek Gissar mountains to the west, the Pamir mountains to the east, and the Hindu Kush to the southeast (Figure 1; e.g., Bourgeois et al., 1997; Gągała et al., 2020). The basin stratigraphy consists of ∼5–10 km of sediments overlying the pre-Triassic crystalline basement that also forms the Tajik Gissar and Uzbek Gissar mountains (Gągała et al., 2020, Figure 2b). The sedimentary sequence begins with Triassic to Oligocene carbonates and clastic deposits from an epicontinental basin including near the base, a layer of upper Jurassic evaporites named the Gaurdak formation (Abdulhameed et al., 2020; Gągała et al., 2020). At the top of the sequence lie synorogenic clastics (mainly conglomerates) derived from the surrounding orogens, which were deposited in the Neogene and followed by the onset of basin inversion and the formation of the thin-skinned fold and thrust belt, which characterizes the present-day morphology of the basin (Abdulhameed et al., 2020; Gągała et al., 2020).

The thrust sheets exhibit an eastward dip in the eastern part of the basin and a westward dip in the western part, with the change occurring across the Yavan syncline (Figure 2; Abdulhameed et al., 2020; Bourgeois et al., 1997; Gągała et al., 2020; McNab et al., 2019). The E-W shortening is primarily confined to the Jurassic—Neogene sedimentary units situated above the Gaurdak evaporite formation, which acts as a detachment layer throughout the basin and lies at the base of the thrust sheets (Gągała et al., 2020; Kufner et al., 2018; Schurr et al., 2014). This thin-skinned deformation is caused by the lateral extrusion of the western Pamir, thought to be due to its gravitational collapse (e.g., Stübner et al., 2013; Kufner et al., 2018). However, other causes of the E-W extension of the Pamir have also been proposed, including radial thrusting on the Main Pamir thrust leading to divergence, and oroclinal bending (e.g., Strecker et al., 1995; Yin et al., 2001; Robinson et al., 2004). Seismic activity within the basin is characterised by earthquakes of generally low magnitude ($M_W < 4.5$), with only a small number of moderate events ($M_W \sim$ 5–6; Kufner et al., 2018; McNab et al., 2019). Most earthquakes occur below the evaporite-bearing layer, indicating aseismic deformation may dominate within the sedimentary cover (Gągała et al., 2020; Metzger et al., 2021). Some earthquakes occur on the detachment horizon where the evaporites have thinned due to diapirism (Kufner et al., 2018). Based on several deep thrust earthquakes and geomorphic mapping of E-W trending folds at the southern edge of the basin, McNab et al. (2019) suggest that the basement is deforming by N-S compression induced by the India-Asia collision, inferring a mechanical decoupling between

the basement and cover. It has also been suggested that stresses relating to lower crustal and mantle delamination and rollback beneath the Pamir and Hindu Kush could be driving deformation within the basement (e.g., Kufner et al., 2018; Sippl et al., 2013).

In the northern part of the basin, a seismic catalogue reveals a cluster of small earthquakes in the centre of the IF, occupying a sub-vertical zone ~4–17 km beneath its surface trace (Figures 2a and 2b; Kufner et al., 2018). The focal mechanisms of the two largest events (M_W 4.7 at 17 km and M_W 3.7 at 14.5 km) are consistent with right-lateral strike-slip (Figure 2a; Kufner et al., 2018). Additionally, the M ~ 5.5 Gissar earthquake (G in Figure 2a) ruptured the western end of the fault in 1989, with a focal mechanism also consistent with right-lateral slip on the IF (Djuraev & Shakirdzanova, 1993). Depth estimates for the Gissar earthquake vary from ~2.5–12 km, but modern estimates from the International Seismological Centre suggest a depth of ~12 km and are consistent within their uncertainties (R. Engdahl et al., 1998; E. R. Engdahl et al., 2020; International Seismological Centre, 2022; Storchak et al., 2020; Weston et al., 2018). Despite its moderate magnitude, the Gissar earthquake had serious effects, causing large landslides in irrigated loess deposits that buried or partially buried several villages and resulted in over 270 fatalities (Djuraev & Shakirdzanova, 1993; Ishihara et al., 1990). These seismic observations suggest that activity on the IF is not limited to the sedimentary cover and indicate the presence of a sub-vertical structure extending into the basement below (Gągała et al., 2020).

The IF forms the southern edge of the Dushanbe Trough, a topographic depression to the south of the Tajik Gissar with the same stratigraphy as the central Tajik Basin but a different structural regime, with fold axes striking ~E-W rather than ~N-S (Figure 2; Gągała et al., 2020). Borehole data, stratigraphic sections and seismic reflection profiles show that the upper Jurassic sediments are much thinner in the Dushanbe Trough and there is no clear evidence for evaporites (Gągała et al., 2020; Leith & Alvarez, 1985). The faults and folds deform the basement and sedimentary cover together, with no evidence of decoupling (Gągała et al., 2020). Gągała et al. (2020) attribute the location of the IF to the tapering out of the Gaurdak evaporites towards the northern edge of the basin.

At the eastern end of the Dushanbe Trough the ~E-W-striking trace of the IF ends, either merging with or continuing beneath a series of overlapping NE-striking basin thrust sheets which directly override the Tajik Gissar, including the Surkhu thrust sheet (STS) and Vakhsh thrust sheet (VTS; Figure 2; Leith & Alvarez, 1985; Bourgeois et al., 1997). Here, sediments are compressed between the Tajik Gissar and the Pamir in a zone of right-lateral transpression and with enhanced seismicity, forming part of the Peter the 1st mountain range (Bourgeois et al., 1997; Kufner et al., 2018).

3. Materials and Methods

3.1. InSAR Data and Method

In this study, we processed data from the European Space Agency's Sentinel-1 Synthetic Aperture Radar (SAR) satellites, specifically from descending track 151 (D151) and ascending track 71 (A071), acquired in IW swath mode. We conducted a Multi-Temporal InSAR analysis (Supporting Information S1) to derive cumulative time series LOS displacement maps and velocity maps over ~400 km long swaths in the range direction between ~36° and ~39.5° latitude (Figure 3). We process the data with the New Small Baseline Subset (NSBAS) processing chain (Doin et al., 2011, 2015; Grandin, 2015), which is based on the ROIPAC software (P. A. Rosen et al., 2004).

We built robust interferogram networks spanning ~5 years for both the ascending and descending tracks. The networks are a mixture of short (less than 72 days) and long (more than 72 days) temporal baseline interferograms, constructed using radar acquisitions from October 2014 to December 2020 for the ascending track and October 2014–March 2021 for the descending track (Figure S1 in Supporting Information S1). Before unwrapping, the networks contained 464 and 593 interferograms for the ascending and descending tracks, respectively. To unwrap the interferometric phase and increase phase coherence (Bamler & Hartl, 1998; Funning, 2005), we performed several pre-unwrapping steps to assist the unwrapping algorithm. First, we corrected interferograms using empirical phase-elevation relationships (Figure S2 in Supporting Information S1; Doin et al., 2011; Doin et al., 2015; Daout et al., 2019) to reduce phase variability and the fringe rate before unwrapping, thereby enabling us after to unwrap over large areas. Then, we replaced the coherence of the phase by the colinearity measurement (Pinel-Puyssegur et al., 2012), multi-looked the interferograms in eight looks (averaging over 8 pixels in azimuth and 32 pixels in range), and filtered the interferograms with a weighted average of the interferometric phase computed on sliding windows (Doin et al., 2011). To avoid the propagation of unwrapping errors, unwrapping

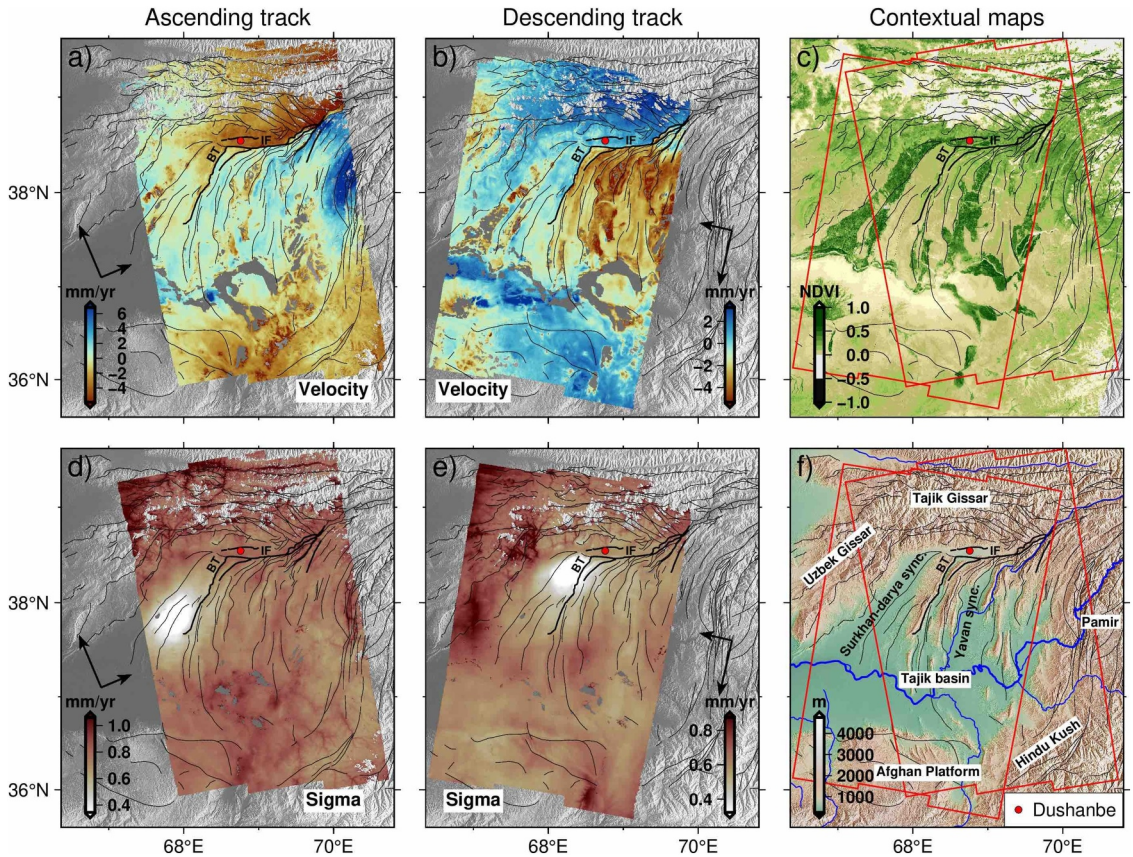

Figure 3. (a) Ascending and (b) descending linear LOS velocity maps overlain on 30 m SRTM DEM hillshade. Negative (red) values indicate relative motion away from the satellite. BT = Babatag thrust, IF = Ilyak fault. (c) Normalized Difference Vegetation Index (NDVI) data from August 2020 (Contains modified Copernicus Sentinel data 2020 processed by Sentinel Hub, accessed through Sentinel Hub EO Browser in 2023). (d) and (e) show 1σ uncertainties for the ascending and descending LOS velocities respectively. (f) Topography (SRTM 30 m DEM) with major rivers in blue, sync = syncline. On all maps, thin black lines are faults after Dedow et al. (2020) and Abdulhameed et al. (2020), and thick black lines highlight active faults discussed in this study. The red point corresponds to Dushambe city. In context maps (c) and (f), red polygons show footprints of the processed radar scenes.

integration paths were imposed based on the amplitude of the filtered phase (Grandin et al., 2012). They, therefore, start in areas of high filtered colinearity and progress into areas of lower filtered colinearity (Grandin et al., 2012). For some interferograms, we also manually defined high-priority paths to guide the algorithm and reduce unwrapping errors (Grandin et al., 2012). After unwrapping the filtered phase, we then computed the phase difference between the smoothed unwrapped phase and less-strongly filtered interferograms obtained from an adaptive filter. The residual high-frequency signal was assumed to be between -π and +π and added back to the smooth unwrapped phase. To reconstruct the full unwrapped phase, the empirical corrections were also reintroduced after unwrapping (Daout et al., 2019). This approach allowed us to unwrap successfully over a large region whilst reducing errors and preserving sharp phase gradients (N. Dodds et al., 2022).

Subsequently, following the approach of N. Dodds et al. (2022), we jointly corrected unwrapped interferograms for a linear ramp and tropospheric phase delays using the ECMWF ERA-5 atmospheric model (Daout et al., 2020; Doin et al., 2009; Hersbach et al., 2020; Jolivet et al., 2011). The linear ramps we remove in this step are likely related to residual signals such as ionosphere, unaccounted-for orbital effects, large-scale plate motion, or solid earth tides (N. Dodds et al., 2022; Lemrabet et al., 2023). We performed a statistical assessment of this correction, which found that the model predicts the tropospheric phase component successfully, with average correlation coefficients between the models and the data of 0.78 and 0.81 for ascending and descending tracks, respectively (Figures S2–S9 in Supporting Information S1; N. Dodds et al., 2022).

Phase-delay time series, $\phi_l(t)$, were generated for each pixel l using the NSBAS method (Doin et al., 2015). Following the approach of Daout et al. (2017), we initially detected residual unwrapping errors through a visual

examination of the interferograms. We calculated the root mean square (RMS) between each interferogram's measured phase and the differential phase reconstructed from the time series analysis (Equation 6 in Text S1.4 in Supporting Information S1; López-Quiroz et al., 2009; Doin et al., 2015). To identify error-prone interferograms and locate the errors, we computed deviation maps for each interferogram (Figure S10 in Supporting Information S1). Using these maps, we specified priority paths across error-prone regions, which were then used in subsequent iterations of the unwrapping procedure to remove these errors. Interferograms with persistent errors were removed during this iterative unwrapping process. During the time series analysis, residual unwrapping errors were further detected and corrected via an iterative method (Figure S11 in Supporting Information S1; Doin et al., 2015; López-Quiroz et al., 2009). The final RMS values were relatively low, with the maximum for any interferogram being around 0.75 radians for the ascending track and 0.6 radians for the descending track.

The LOS displacement of the ground over the ~5 years study period was primarily characterized by linear trends linked to interseismic deformation, along with seasonal patterns likely due to atmospheric seasonal delays or hydrological effects in mountainous, riverine, and reservoir areas. To model these variations, we fitted sine and cosine functions with annual periods, as well as a linear trend for each pixel (Equation 8 in Text S1.5 in Supporting Information S1; Daout et al., 2017, 2023). Additionally, we computed the LOS velocity error for each pixel and parameter (Equation 9 and Figures S12 and S13 in Text S1.5 of Supporting Information S1; Daout et al., 2017; Daout et al., 2023).

To address issues of phase bias related to changes in soil moisture and vegetation documented in previous studies (e.g., Ansari et al., 2021; Daout et al., 2020; De Zan et al., 2014; Maghsoudi et al., 2022), we incorporated longer period interferograms into our networks and removed interferograms with temporal baselines less than 32 days from our final time series analysis (Daout et al., 2020, 2023; De Luca et al., 2022; Mathey et al., 2022). We also masked areas potentially affected by bias from the final LOS velocity maps by removing pixels with average temporal baselines of <3 months (Mathey et al., 2022). We additionally cleaned the final maps based on the posterior numerical uncertainties from the time series inversion and the parametric temporal decomposition to remove high-uncertainty pixels (Figure S13 in Supporting Information S1).

After this cleaning step, we decomposed the LOS velocity maps (Figure 3) into vertical and eastward velocities (V_U and V_E, Text S1.8 in Supporting Information S1; Wright, Parsons, England, & Fielding, 2004; Daout et al., 2023). The available GNSS velocities are sparse (particularly in the southern part of the study area) and irregular with high uncertainties in the vertical component or no vertical component (Ischuk et al., 2013; Kufner et al., 2021; Metzger et al., 2020; Mohadjer et al., 2010; Zubovich et al., 2010). Therefore, we referenced the LOS rate maps internally to a section of the basin interior to the west of the BT where the spatial and temporal coherence is high (red rectangular box in Figure 4), rather than tying them to stable Eurasia using the GNSS velocity field.

We also chose not to use the GNSS velocity field to add additional constraints in the spatial decomposition. Instead, we assume the northward component of the linear velocity field is negligible—InSAR LOS measurements are relatively insensitive to the limited N-S displacements in the study area, due to the near-polar orbit of Sentinel-1 satellites and because of the overall E-W orientation of the strike-slip faults and N-S orientation of thrust faults. To evaluate the robustness of the 2-dimensional assumption, we performed two synthetic tests (Figures S15 and S16, Text S1.8 in Supporting Information S1), which demonstrate that the 2D decomposition introduces a small bias into the vertical velocity field and sometimes also the eastward velocity field - but in the near-field of the faults the bias mostly affects the vertical measurements. Eastward velocities induced by the IF are unaffected by the 2D simplification, but vertical velocity measurements at the fault may be slightly underestimated on the order of ~0.1 mm/yr, if the IF accommodates N-S shortening. The fault deformation rates most affected are vertical velocity measurements across NE-SW striking faults with a significant N-S component, such as the thrusts in the Tajik Basin where the vertical may be underestimated on the order of a few tenths of a mm/yr at the fault. However, the magnitude of the bias from the 2D simplification remains limited when compared to the overall amplitude of deformation observed across the fold and thrust belt.

In order to analyse localized ground deformation, we also applied a high-pass filter to the east and vertical velocities to produce maps showing only the shorter wavelength signals (Figure 5). To produce these maps, we subtracted a Gaussian low-pass filter with a 2 km window size from the decomposed eastward and vertical

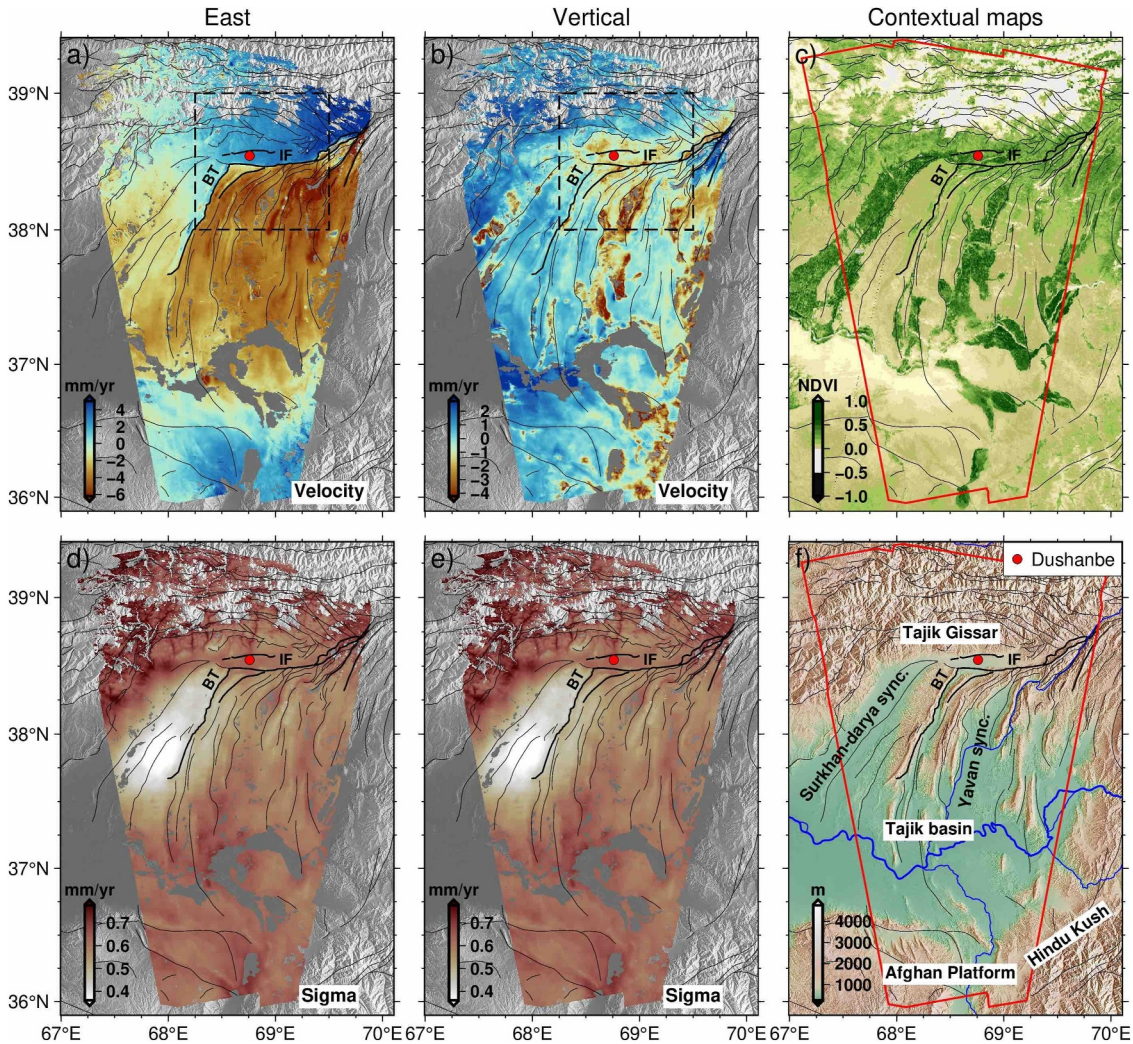

Figure 4. As in Figure 3 but for (a) eastward and (b) vertical velocities obtained from the spatial decomposition of the ascending and descending linear velocities. Velocities are relative to the reference zone (red rectangle). Negative (red) values indicate relative westwards motion in (a) and relative downwards motion in (b).

velocity maps. The resulting high-pass filtered maps reveal deformation relating to rock slope instabilities, soil creep, water extraction, and fault creep.

3.2. DEM Generation and Scarp Measurement

We constructed Digital Elevation Models (DEMs) from Pléiades satellite imagery of the Dushanbe Trough acquired between 2012 and 2021. We process eight pairs of panchromatic stereo images using Agisoft Metashape software to build 3D point clouds and DEMs with a horizontal spatial resolution of <1.5 m.

We use these DEMs to map the tectonic geomorphology of the Dushanbe Trough, to identify Quaternary fault scarps and measure their offset. We extract elevation profiles approximately perpendicular to scarps, fit linear models to the hanging wall and footwall, and calculate the difference in their heights at the inferred location of the fault (see Text S3 in Supporting Information S1). Within Dushanbe city, we draw profiles along major N-S oriented roads to avoid the impact of buildings on the elevation data.

4. Results

With our bespoke processing approach, we produce rate maps with a horizontal resolution of ∼130 m, around three times higher resolution than the previously published velocity maps of the region and with more continuous

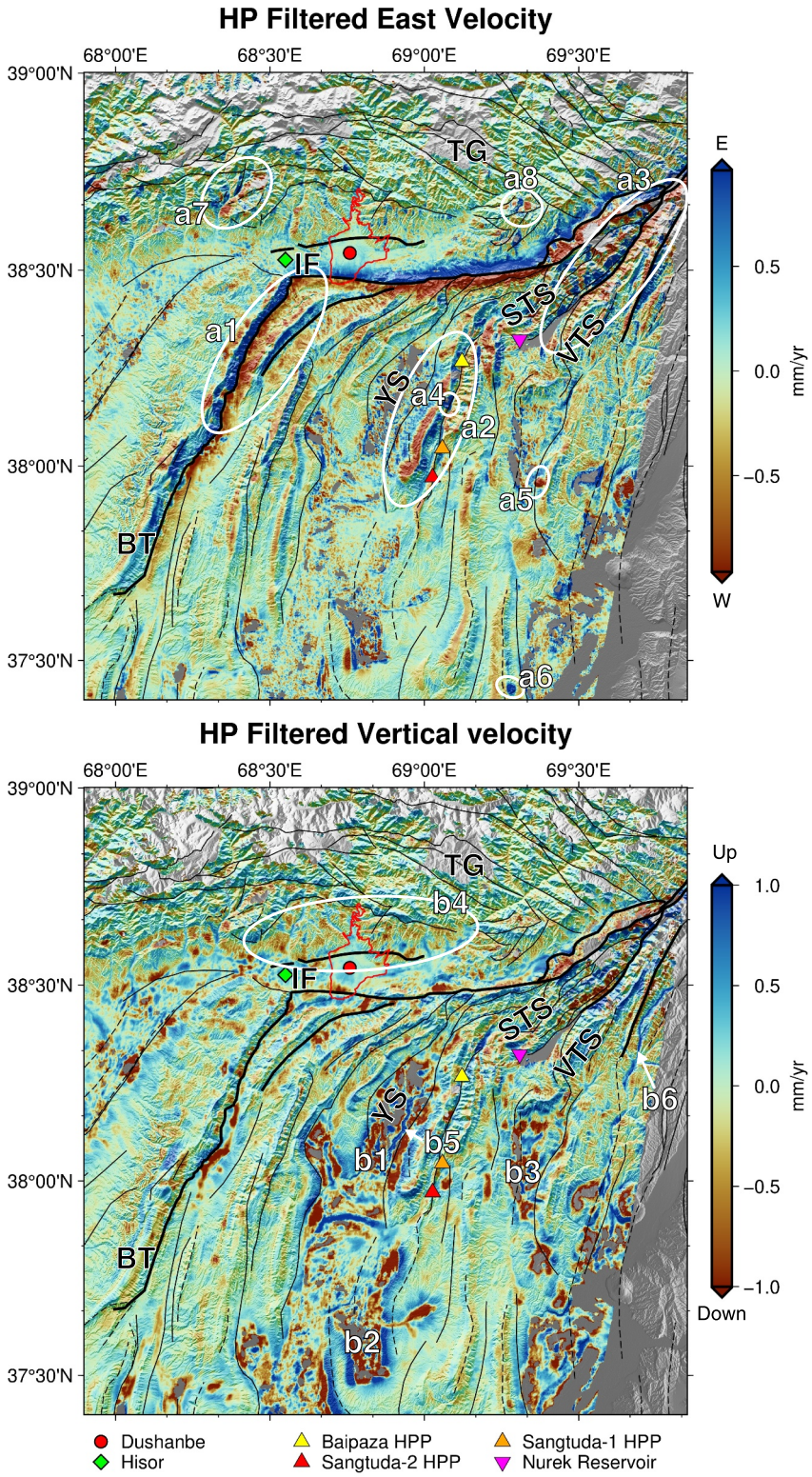

Figure 5. Upper and lower panels show high-pass filtered east and vertical velocity maps respectively, shaded by the gradient of the SRTM 30 m DEM. Solid and dashed black lines are faults and folds after Dedow et al. (2020) and Abdulhameed et al. (2020), and thick black lines highlight active faults discussed in this study. Geological features labelled in black: BT = Babatag Thrust, IF = Ilyak Fault, TG = Tajik Gissar, YS = Yavan Syncline, STS = Surkhu Thrust Sheet, VTS = Vakhsh Thrust Sheet. HPP = Hydro Power Plant. Features discussed in the text are labelled in white and in some cases circled in white.

coverage, especially in the Tajik Gissar and NE Tajik Basin. The LOS velocity maps are presented in Figure 3. In these maps, negative values (red) indicate relative motion away from the satellite. The LOS velocities have average posterior numerical uncertainties (derived from Equation 9 in Text S1.5 of Supporting Information S1) of 0.6 mm/yr and 0.8 mm/yr for the ascending and descending tracks, respectively. Even after cleaning based on uncertainties and the average temporal baseline, we retain good data coverage, providing an unprecedented continuous estimate of surface deformation in our study area.

The LOS velocity maps show the westward motion of the eastern two-thirds of the Tajik Basin relative to the Tajik Gissar and the Afghan Platform. In the north and west of the basin, very high velocity gradients are co-located with the right-lateral IF and the BT, respectively. The descending LOS velocity map shows relative motion away from the satellite to the south of the IF (~4–5 mm/yr relative to the north) and east of the BT (~2–3 mm/yr relative to the west). In contrast, the ascending LOS velocity map shows relative motion towards the satellite to the south of the IF (~4–6 mm/yr relative to the north) and east of the BT (~2–3 mm/yr relative to the west). The ascending track map also captures the motion of the western edge of the Pamir mountains, showing up to ~10 mm/yr of motion towards the satellite relative to the lowlands of the basin. This signal indicates uplift, westward motion (consistent with the westward collapse of the Pamir) or a combination of the two. Within the basin interior, both tracks show localized patches moving rapidly away from the satellite at several mm/yr and up to ~16 mm/yr within the valley of the Surkhan-darya syncline (Figure 3f). These patches correspond to agricultural areas (see NDVI map in Figure 3c), and are likely a subsidence signal caused by water extraction.

The derived vertical and eastward velocity maps are presented in Figure 4, with average uncertainties of 0.8 and 0.6 mm/yr, respectively. These maps show the velocities relative to a reference zone to the west of the BT (red rectangle in Figure 4). We note that these velocity fields are affected by the limited N-S component of the InSAR signal due to the 2D simplification (Figures S15 and S16 in Supporting Information S1), though the impact is minimal in comparison to the scale of the deformation and they should be considered good approximations of the true eastward and vertical velocities. We highlight below where N-S deformation may have a significant impact on measurements.

The east rate map confirms the sharp velocity contrast in the north and east of the basin, corresponding to right-lateral motion across the IF and convergence on the westward-dipping BT. The vertical rate map is dominated by the signal from the subsiding fields (especially within the Yavan syncline in the center of the basin) but also reveals a longer wavelength signal of relative subsidence of the basin sediments compared to the surrounding mountains.

In the following sections, we further examine tectonic deformation signals in our study region (black boxes in Figures 4a and 4b), the north of the Tajik basin and the Dushanbe Trough, combining our InSAR measurements with geomorphic mapping. We then consider the implications of our results for the tectonics of the Tajik Basin, and for seismic hazard in Dushanbe.

4.1. The Ilyak Fault (IF)

The eastward velocity map reveals a sharp change in surface velocity on the IF, consistent with shallow creep on a right-lateral strike-slip fault (Figures 4 and 6). To quantify the strike-slip rate and its variation along strike, we extracted nine adjacent velocity profiles across the IF, each 7.5 km wide and 80 km long (Figure 7). We then smoothed the data in each profile and inverted for the strike-slip rates and locking depths using a simple arctangent model, assuming strike-slip in a homogeneous elastic half-space (Text S2 and Equation 11 in Supporting Information S1; Savage & Burford, 1973; Turcotte & Schubert, 2014). The modelled strike-slip rate is ~8.1–8.7 mm/yr at the eastern end of the IF (profiles 7–9), decreasing to ~6.7–7.1 mm/yr in the central part of the fault (profiles 4–6). Modelled locking depths for profiles 5–9 are very low (0–300 m), confirming very shallow creep. Upper Jurassic rocks, which either contain or stratigraphically neighbor the Gaurdak evaporite formation, crop out in multiple locations along this section of the IF, suggesting that this layer may control the creep behavior (Abdulhameed et al., 2020; Gągała et al., 2020).

The high-pass filtered velocity map (Figure 5) confirms localized velocity gradients on the fault, consistent with shallow creep. A series of streams crossing the IF at the longitude of profile 6 were identified in our high-resolution DEM mapping (Figure 8). These streams have been deflected right-laterally by ~100–500 m, matching the localized strike-slip deformation measured by InSAR (Figure 8).

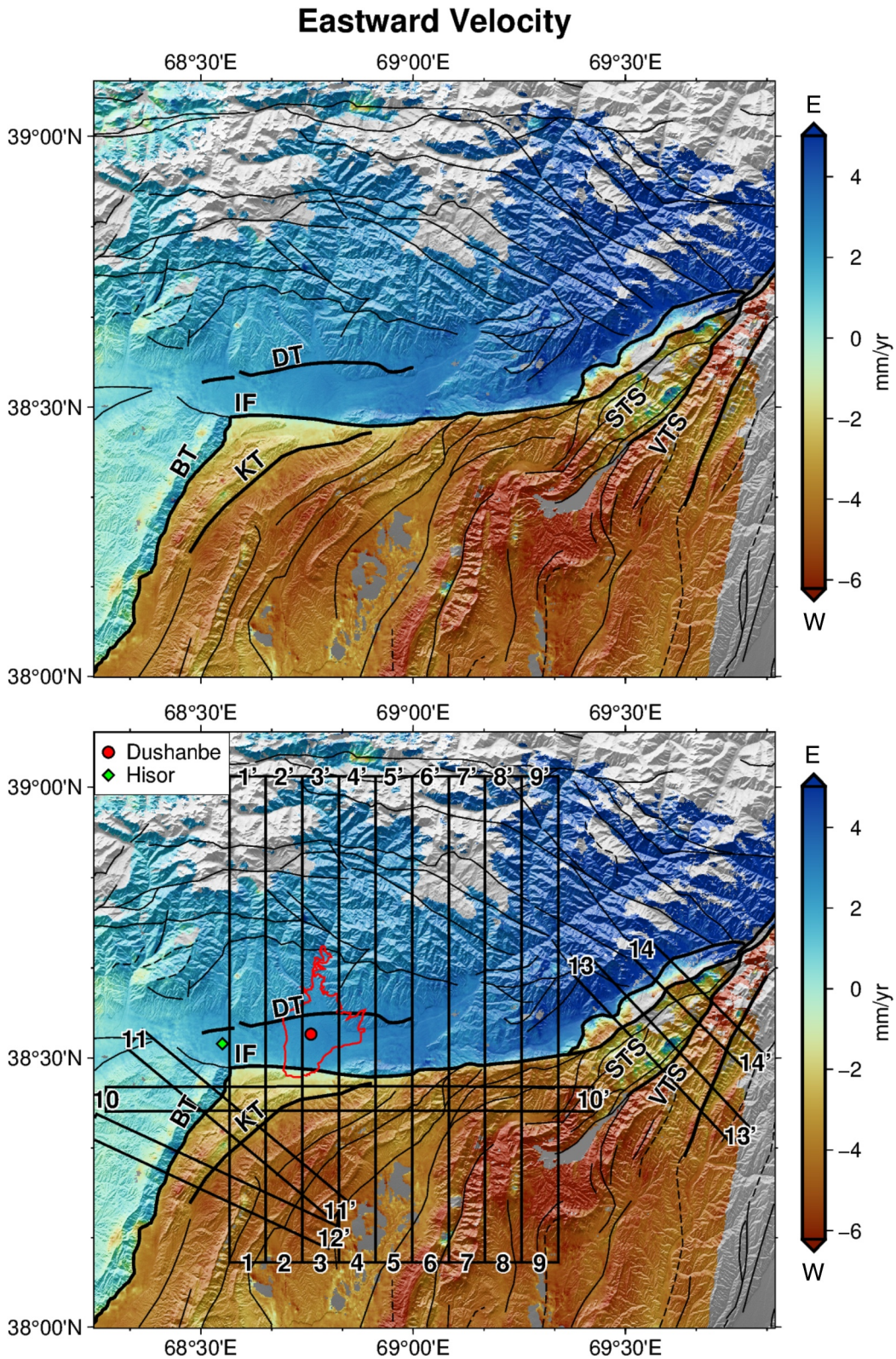

Figure 6. Eastward velocity map, referenced to the basin interior to the west of the Babatag Thrust (BT), of the Ilyak fault and surroundings, shaded by the gradient of the SRTM 30 m DEM. Solid and dashed thin black lines are faults and folds after Dedow et al. (2020) and Abdulhameed et al. (2020). Thick black lines = active faults discussed in this study. Rectangles show locations of profiles in Figures 7 and 11, and 12. KT = Karchitau thrust, IF = Ilyak fault, DT = Dushanbe Trough thrust, BT = Babatag thrust. Red polygon = Dushanbe urban area from OpenStreetMap contributors (2023).

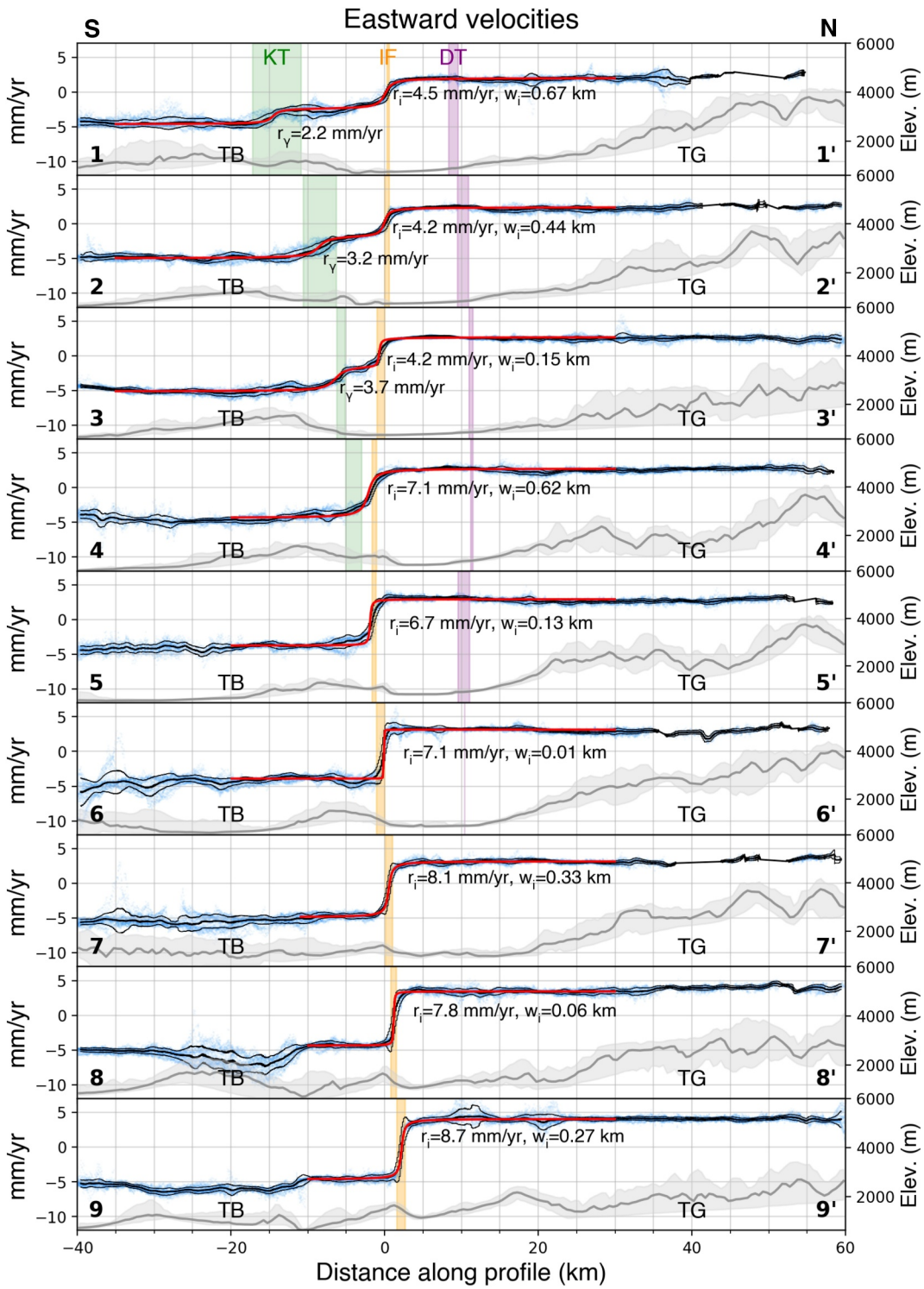

Figure 7. Eastward velocity profiles across the Ilyak fault (positive direction indicates relative eastward motion) marked as black rectangles in Figure 6. Blue points show eastward velocity measurements. The thick black line represents the median computed over ~1 km-wide sliding windows, and the thin black lines represent $\pm 1\sigma$ around that median. Fault extents (defined through remote mapping) of the Karchitau thrust (KT), Ilyak fault (IF), and Dushanbe Trough thrust (DT) are shown in green, orange, and purple, respectively. Red lines show best fitting arctangent models for the IF and the KT, where r_i and w_i are the modelled strike-slip rate and modelled locking depth on the IF, respectively, and r_γ is the modelled E-W rate on the KT. Formal 1σ model uncertainties are $\leq$0.02 mm/yr for all rates, and $\leq$0.01 km for all locking depths. SRTM 30 m elevation data is plotted in grey (dark line = median elevation). TB = Tajik Basin, TG = Tajik Gissar.

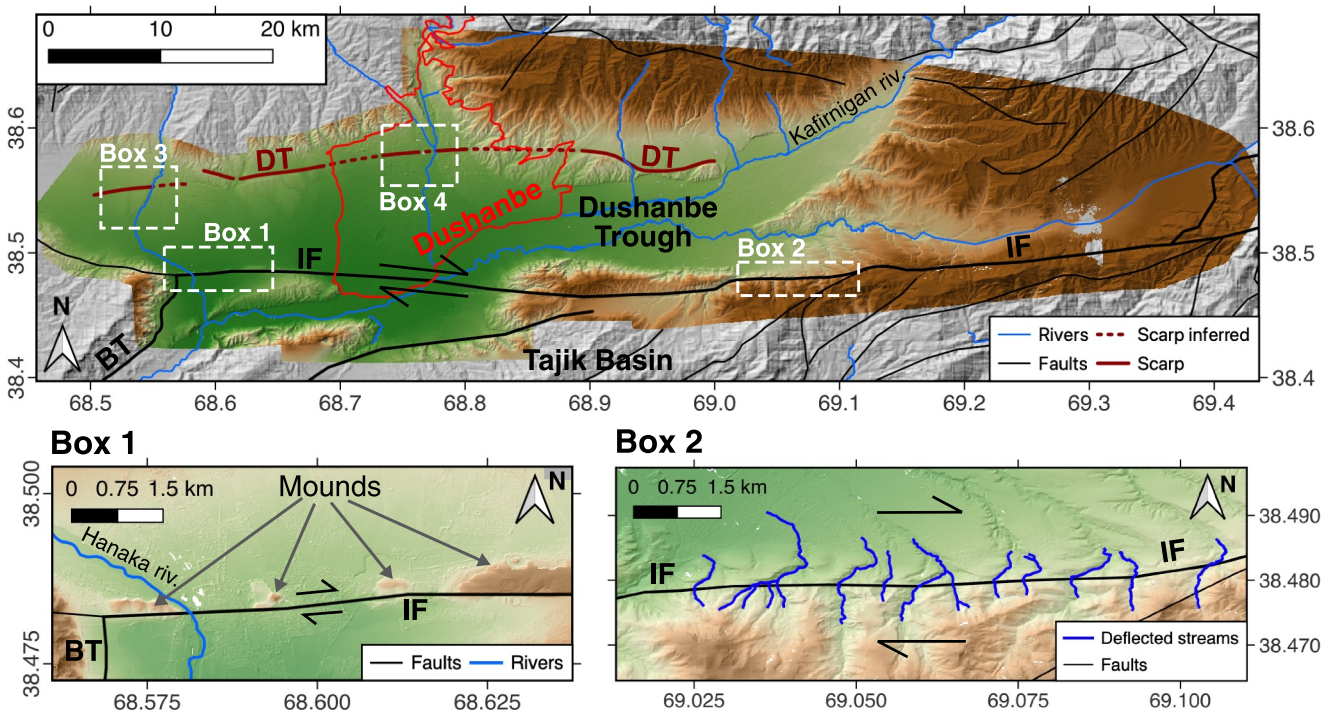

Figure 8. Pléiades-derived DEM of the Dushanbe Trough. DT = Dushanbe Trough thrust, IF = Ilyak fault, BT = Babatag thrust. Background topography (grey) from SRTM 30 m DEM. Rivers and red polygon showing Dushanbe administrative boundary from OpenStreetMap contributors (2023). Solid thin black lines are faults after Dedow et al. (2020) andAbdulhameed et al. (2020). Thick black lines highlight active faults discussed in this study. Thick red line = scarp mapping for the Dushanbe trough thrust. Box 1: Mounds along the Ilyak fault trace. Box 2: Offset streams along the Ilyak fault trace. Boxes 3 and 4 correspond to regions shown in 13.

The vertical velocity map reveals minimal deformation across the IF compared to the high horizontal velocity changes (Figures 9 and 10). For the vertical velocity profiles, we estimate the velocity contrast at the fault using a simple step function, which we fit to data very close to the fault (within ~5–10 km of the fault trace). In the eastern part of the IF (profiles 7–9) we measure a ~1 mm/yr vertical velocity change, with the southern side of the fault uplifting relative to the north. In this eastern section, multiple South or SE dipping thrust sheets are stacked up against the southern side of the IF, forming the high topography on the southern side of the fault (e.g., Figures 2c and 7; Abdulhameed et al., 2020; Gągała et al., 2020). This uplift signal most likely originates from motion on a dipping thrust, which merges with the main strike-slip structure at the surface, as it is correlated with the morphology of the folds at the surface (Figure 8). In the center of the IF (profiles 4–6), where the basin folds and thrusts strike at a higher angle to the fault trace, there are subdued undulations in vertical surface velocities, but there is no measurable vertical velocity contrast across the IF, suggesting that the IF does not accommodate shortening in this segment.

Further to the west, the IF passes through the southern part of the valley in which Dushanbe is situated. We found no geomorphic evidence of faulting within the youngest fan sediments in this section at the resolution of our DEMs (e.g., Figure 8). At the southwestern end of the Dushanbe Trough, the IF forms the sharp northern boundary of a ~180 m high mountain for 5 km, and then enters the southern part of the Hanaka river valley where four small uplifted blocks (~0.5–2 km wide and tens of meters high) follow the fault trace (Figure 8, Box 1). We suggest that these mounds are likely compressional push-up structures induced by predominantly strike-slip activity on the IF.

In most of the profiles 1–9, less prominent E-W velocity gradients on the Tajik basin folds and faults are apparent to the south of the IF (Figure 7 and profile 10 in Figure 11). To the west of profile 5, the ENE to NNE striking Karchitau thrust (KT) emerges from the IF. The E-W deformation is partitioned between the two faults, and by profile 3, two distinct steps in the surface velocities are visible. These steps become progressively more separated as the trace of the KT moves southwards.

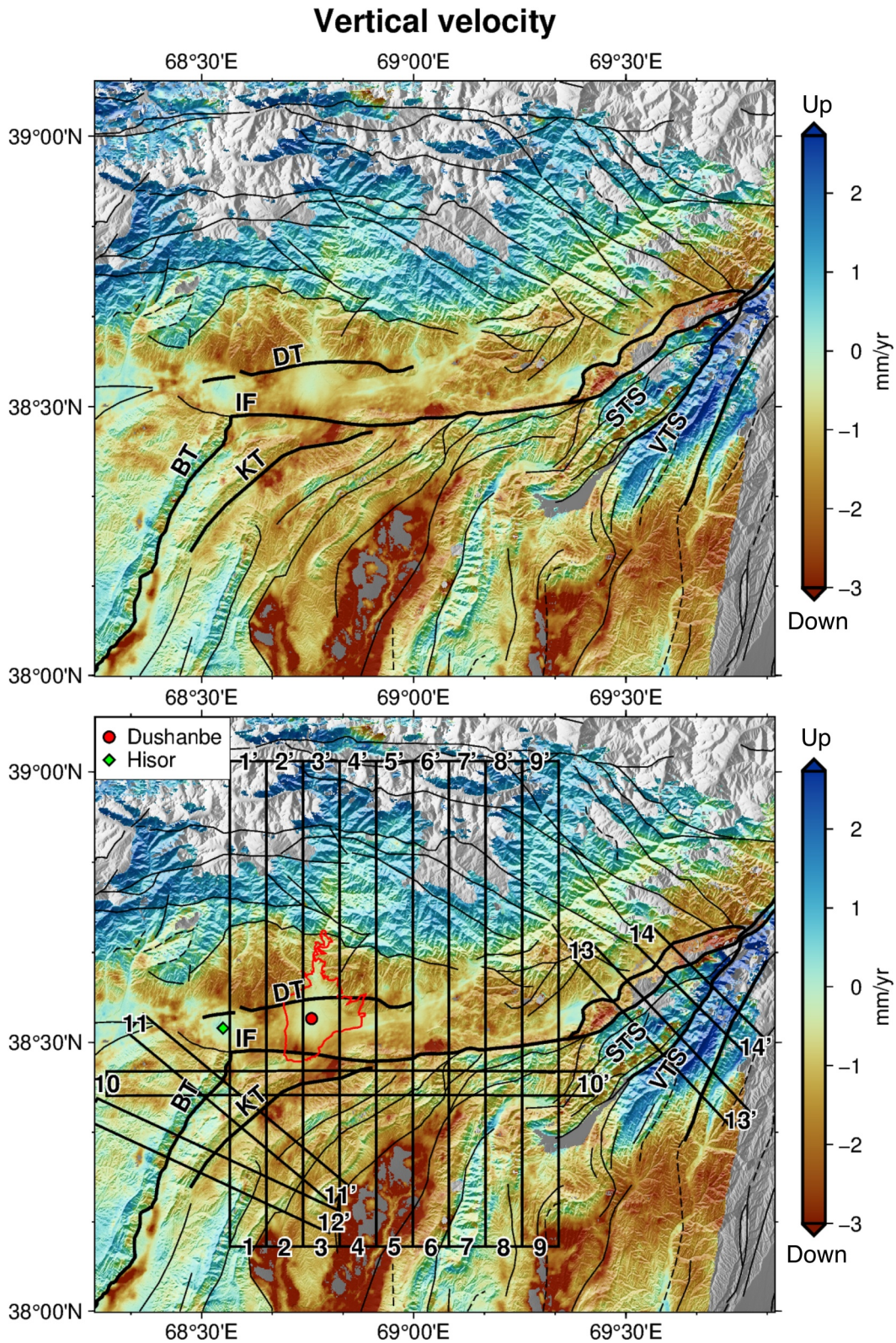

Figure 9. Vertical velocity map, referenced to the basin interior to the west of the Babatag Thrust (BT), of the Ilyak fault and surroundings, shaded by the gradient of the SRTM 30 m DEM. Solid and dashed thin black lines are faults and folds after Dedow et al. (2020) and Abdulhameed et al. (2020). Thick black lines = active faults discussed in this study. Rectangles show locations of profiles in Figures 10–12. Red polygon = Dushanbe urban area from OpenStreetMap contributors (2023).

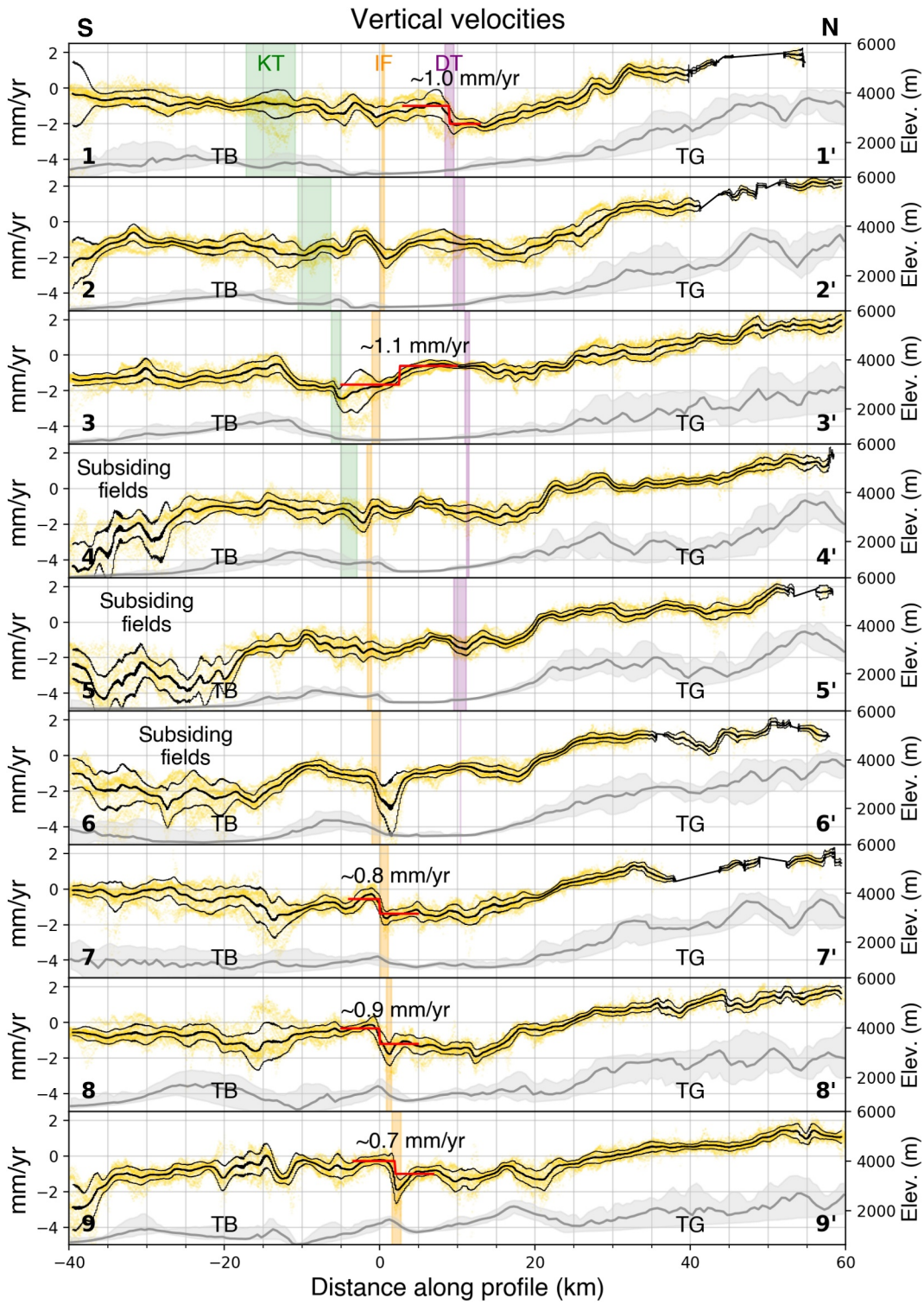

Figure 10. Vertical velocity across the Ilyak fault (positive direction indicates relative upwards motion) corresponding to profiles in Figure 9. Yellow points show vertical velocity measurements. The thick black line represents the median computed over ~1 km-wide sliding windows, and the thin black lines indicate $\pm 1\sigma$ around that median. Fault extents (defined through mapping) of the Karchitau thrust (KT), Ilyak fault (IF), and Dushanbe Trough thrust (DT) are shown in green, orange and purple, respectively. Red lines show step functions fitted across the IF or the DT labelled with the estimated vertical rate. SRTM 30 m elevation data is plotted in grey (dark line = median elevation).

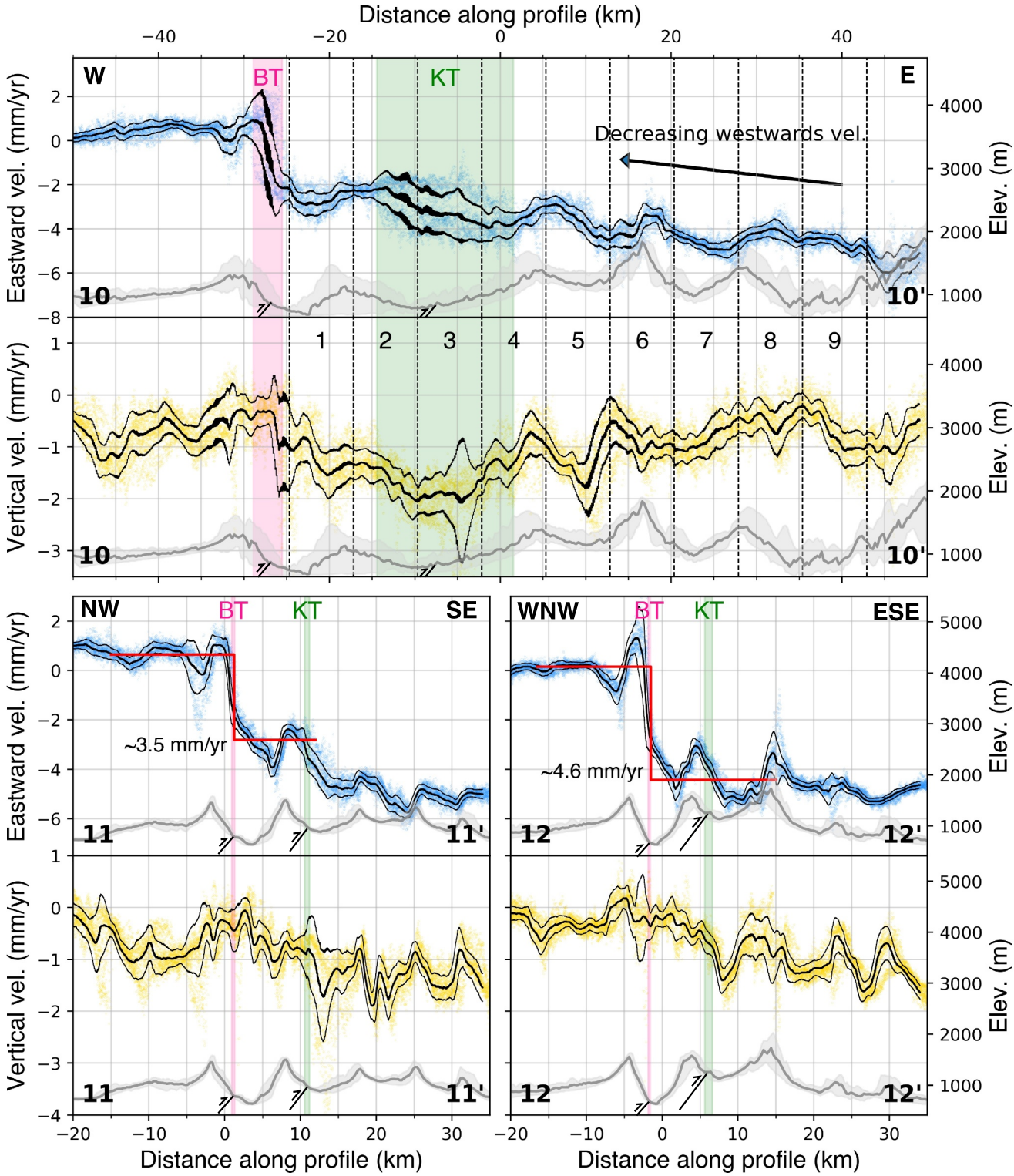

Figure 11. East and vertical velocity profiles from the Tajik Basin corresponding to profiles 10–12 in Figures 6 and 9. Profile 10 is parallel to and immediately south of the IF. Profiles 11 and 12 focus on the Babatag Thrust (BT) and Karchitau Thrust (KT). Blue and yellow points show eastward and vertical velocity measurements, respectively. In each profile, the thick black line represents the median computed over ~1 km wide sliding windows, and the outer two thin black lines indicate $\pm 1\sigma$ around that median. Red lines show step functions fitted across the BT labelled with estimated shortening rates. Fault extents of BT and KT are shown in pink and green, respectively, and schematic approximations of their geometry are in black. Elevation data (SRTM 30 m DEM) is plotted in grey (dark line = median elevation).

We incorporate the KT into our arctangent model of the IF by approximating it as a strike-slip fault with respect to the eastward velocity data, but we note that some of the KT's eastwards velocity signal does originate from thrust deformation, particularly in profiles 1 and 2 where it crosses the profile obliquely (Figure 7). We therefore do not quote a modelled locking depth for the KT, but assume the deformation rate from our simple model is still a reasonable approximation. We find that the strike-slip rate on the IF decreases to ∼4.2–4.5 mm/yr (profiles 1 to 3) in the west as the KT accommodates ∼2.2–3.7 mm/yr of E-W deformation as oblique slip on a ∼NW dipping fault plane. In these western profiles the surface velocity contrasts across the IF are less sharp than in the east, and our models yield a slightly larger locking depth of ∼300–700 m (profiles 1–4). This is probably because the basin folds and thrusts are oblique to the strike of the IF in this section, and the evaporite bearing Upper Jurassic sediments do not crop out at the surface along the fault, according to the geological map (Abdulhameed et al., 2020; Gągała et al., 2020). As such, creep may not reach the surface in the west of the IF because the evaporite horizon is buried. Base salt contours interpreted from seismic sections in Gągała et al. (2020) also show that the base of the evaporite layer is deeper and flatter in the western part of the IF than in the east.

Vertical velocity profile 3 (Figure 10) shows ∼1 mm/yr of uplift of the sediments to the north of the IF. However, examining the vertical velocity map (Figure 9), this profile captures the Dushanbe urban area, which appears to be subsiding less rapidly than the surrounding fields and the low-lying hills to the NW and NE. We are uncertain if this signal is tectonic or the result of water extraction outside of the urban areas causing increased subsidence. The other western profiles show subdued undulations with amplitudes of <1 mm/yr in the vertical velocity near the IF, but there is no significant uplift signal associated with shortening.

4.2. Slip Partitioning Between the Ilyak Fault (IF) and the Tajik Fold and Thrust Belt

In the southwestern corner of the Dushanbe Trough, horizontal surface velocities on the IF end abruptly as slip transfers onto the N–NNE-striking, westward-dipping BT (Figure 6). Within our study area, located in the northern part of the basin, we observe an abrupt change in east–west surface velocities across the mapped trace of the Babatag Thrust, which accommodates more shortening than any of the other basin thrusts (profiles 10–12 in Figures 6 and 11).

We estimate shortening rates across the BT by fitting a simple step function in horizontal velocity profiles 11 and 12 after smoothing them with a sliding median filter (Figure 11). The estimated shortening across the BT is on the order of ∼4–5 mm/yr, with some lateral variations along the fault. The sharpness of the horizontal velocity step at the BT suggests very shallow creep on the evaporite-bearing Upper Jurassic Gaurdak Formation, which forms the base of the thrust sheet (Abdulhameed et al., 2020; Gągała et al., 2020). Vertical velocity contrasts (Figure 11) are of smaller amplitude and noisier than the E–W velocities, showing up to ∼0.5 mm/yr of uplift within the ∼5–10 km around the BT. In the northern part of the basin (Figure 6), the KT also plays a role in accommodating E-W deformation—on the order of ∼2 mm/yr in profile 11. The short-wavelength undulations in the E–W velocities on either side of the BT (Figure 11) may be related to localized surface processes discussed in Section 4.5, likely the E–W divergence of ridge crests first identified by Metzger et al. (2021), or possibly residual tropospheric delays. We also attempted to model the interseismic displacements on the BT using dislocations in an elastic half-space, but the limited amplitude of the observed vertical displacements across the fold and thrust belt prevented satisfactory fits. This may indicate that non-elastic rheologies must be accounted for in modelling or that vertical measurements may be biased due to the neglected north–south component resulting from the 2D simplification (Figure S16 in Supporting Information S1).

A profile oriented in the E-W direction across the Tajik Basin and located immediately south of the IF reveals a trend in the westward velocity, which decreases from the eastern side of the basin towards the BT (profile 10, 11). This trend is a result of the basin folds and thrusts accommodating greater portions of the deformation as slip is transferred to them from the IF. The velocity undulates around this overall trend on the individual deforming faults and folds, such as the KT, as well as due to superficial processes like soil creep (Figure 14, see Section 4.5).

At the eastern end of the IF, the Surkhu thrust sheet (STS) and Vakhsh thrust sheet (VTS) overthrust the basement of the Tajik Gissar in a right-lateral transpressional zone (e.g., Figure 2b; Leith, 1985). It is unknown whether the strike-slip IF ends here, merges with the thrust sheets, or continues beneath them as a separate structure. Figure 12 shows two profiles across these thrust sheets. The E-W velocity contrast between the basin thrusts and the mountains (Tajik Gissar) is ∼7–9 mm/yr, with the velocity change distributed across a ∼ 5 km wide sliver of basin sediments (cf. Figure 2b). Profiles 13 and 14 show the thrust sheets to be uplifting at ∼2–4 mm/yr inter-

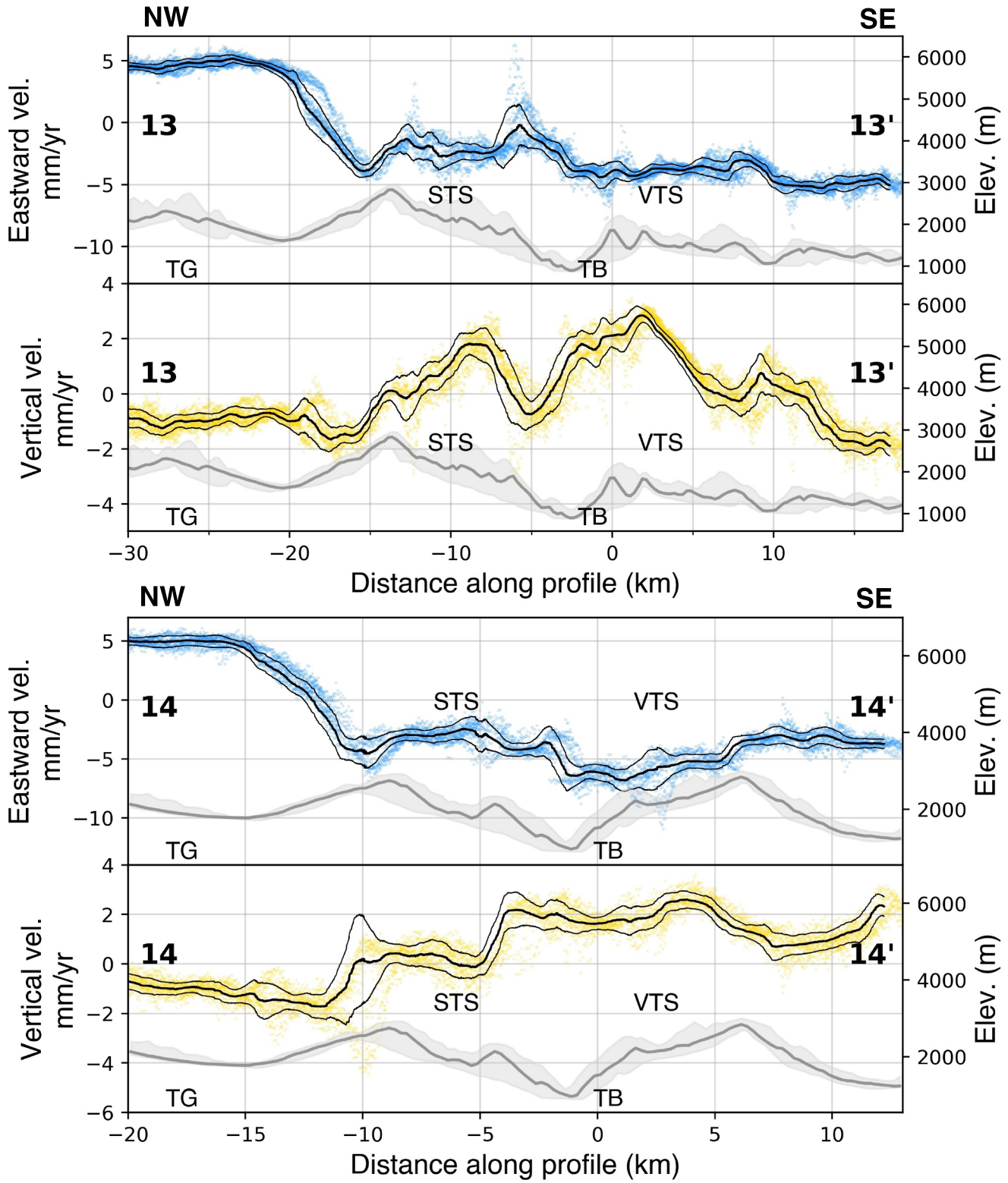

Figure 12. East and vertical velocity profiles of the northeast Tajik Basin (TB) and southeast Tajik Gissar (TG), showing the Surkhu thrust sheet (STS) and Vakhsh thrust sheet (VTS), and corresponding to profiles 13 and 14 Figures 6 and 9. Blue and yellow points show eastward and vertical velocity measurements, respectively. In each profile, the central thick black line represents the median computed over ~0.8 km wide sliding windows, and the outer two thin black lines indicate $\pm 1\sigma$ around that median. Elevation data (SRTM 30 m DEM) is plotted in grey (dark line = median elevation).

seismically, with the VTS over-thrusting the STS as evidenced by the stepped vertical velocity in profile 14. We note that a significant component of the shortening on these NE striking thrusts is likely in the N-S direction, so the vertical measurement in particular may be slightly underestimated due to the 2D approximation made in the spatial decomposition (Figure S16 in Supporting Information S1). The sharp changes in horizontal surface velocities are consistent with shallow creep on the basal evaporites. The major steps in vertical and eastward velocity do not always occur at the same distance along the profiles, suggesting that the thrust and strike-slip components are sometimes partitioned between different structures.

4.3. Vertical Signal in the Tajik Gissar

In the vertical velocity map (Figure 9) and N-S vertical velocity profiles 1 to 9 (Figure 10), large-scale uplift of the Tajik Gissar is apparent, with up to ∼3.5 mm/yr of uplift in the highest mountains relative to the Tajik Basin and Dushanbe Trough. Although the basement thrust at the southern edge of the Tajik Gissar could be active (in some locations, there is some short-wavelength uplift at the topographic front), the dominant uplift signal occurs over a much longer wavelength than we would expect from strain accumulation on thrust faults. We suggest that this long-wavelength vertical signal could result from isostatic uplift due to erosion of the mountains (e.g., Avouac & Burov, 1996; Bullen et al., 2001; Lazear et al., 2013; Vernant et al., 2013) or possibly deglaciation (Liu & Jónsson, 2025). We note that a small proportion of this vertical signal might be attributed by N-S deformation, due to the assumptions of our modelling approach. We also cannot rule out residual tropospheric delays as a possible origin of this signal, although the interferograms were corrected using atmospheric models and the time series analysis, combined with the horizontal/vertical decomposition of the LOS velocity maps, helped to reduce stratified and turbulent atmospheric artefacts. Residual vertical velocity–elevation correlations estimated over two different regions (Figure S17 in Supporting Information S1) suggest minimal correlation between velocity and topography, particularly within the Tajik Basin (Figure S17A in Supporting Information S1). The strongest correlation is observed in an area spanning part of the Tajik Gissar and the north of the Dushanbe Trough, with approximately 0.8 mm/yr of vertical motion for 1,000 m of elevation change (Figure S17B in Supporting Information S1).

4.4. Dushanbe Trough

Our InSAR velocity maps, combined with our geomorphic analysis and existing geological mapping, allow us to assess potential deformation and active faulting in the Dushanbe Trough, north of the IF trace. There are several geological faults and folds within the Dushanbe Trough (Gągała et al., 2020), and there have previously been local mapping studies of the faults around Dushanbe (personal communication, A. Ischuk, 2024). In this study, we focus on faulting that we can assess remotely from its geomorphic expression in satellite imagery and high-resolution DEMs derived from stereo satellite data (Figure 13).

Two prominent ∼E-W trending ridges are apparent in the Quaternary strata to the east and west of Dushanbe. These ridges are asymmetrical with a steeper northern limb, suggesting they may have formed above a south-dipping thrust fault which we refer to as the Dushanbe Trough thrust (DT). The ridges are truncated by the alluvial fans associated with the rivers that exit the Tajik Gissar into the Dushanbe Trough. Our analysis of high-resolution DEMs reveals evidence of active faulting within these younger alluvial surfaces along-strike of the larger ridges, as detailed in the paragraphs below.

On the west bank of the Hanaka river, near the town of Hisor, the southern side of the fan is uplifted relative to the north with a vertical offset of up to ∼20 m (Figure 13, Box 3, profiles A-A′ and B-B′). We map a ∼250 m wide inactive channel in the hanging wall, which we interpret as a wind gap—a former river channel that was abandoned when hanging-wall uplift blocked the flow (profile D-D′). The scarp is truncated to the east by a younger fan surface, which is undeformed at the resolution of our data set (profile C-C′). We also map uphill-facing thrust scarps, either side of the Varzob river (Figure 13, Box 4). We measure the height of these scarps along N-S oriented roads in Dushanbe city and find them to be ∼7–8 m high (profiles E-E′ and F-F′). The Big Gissar Canal is built on top of these scarps (Figure 13). Further to the east in the next valley along, the Kafirnigan River is oriented approximately parallel to the strike of the fault (Figure 8). Whilst we found some offsets here that could potentially be consistent with faulting, we could not distinguish them from river terracing.

Examining the InSAR vertical velocities, in Profile 1 (Figure 10) an apparent ∼1 mm/yr velocity change is centered on the DT. While the step in vertical velocity could indicate activity on the DT, it is not present in the

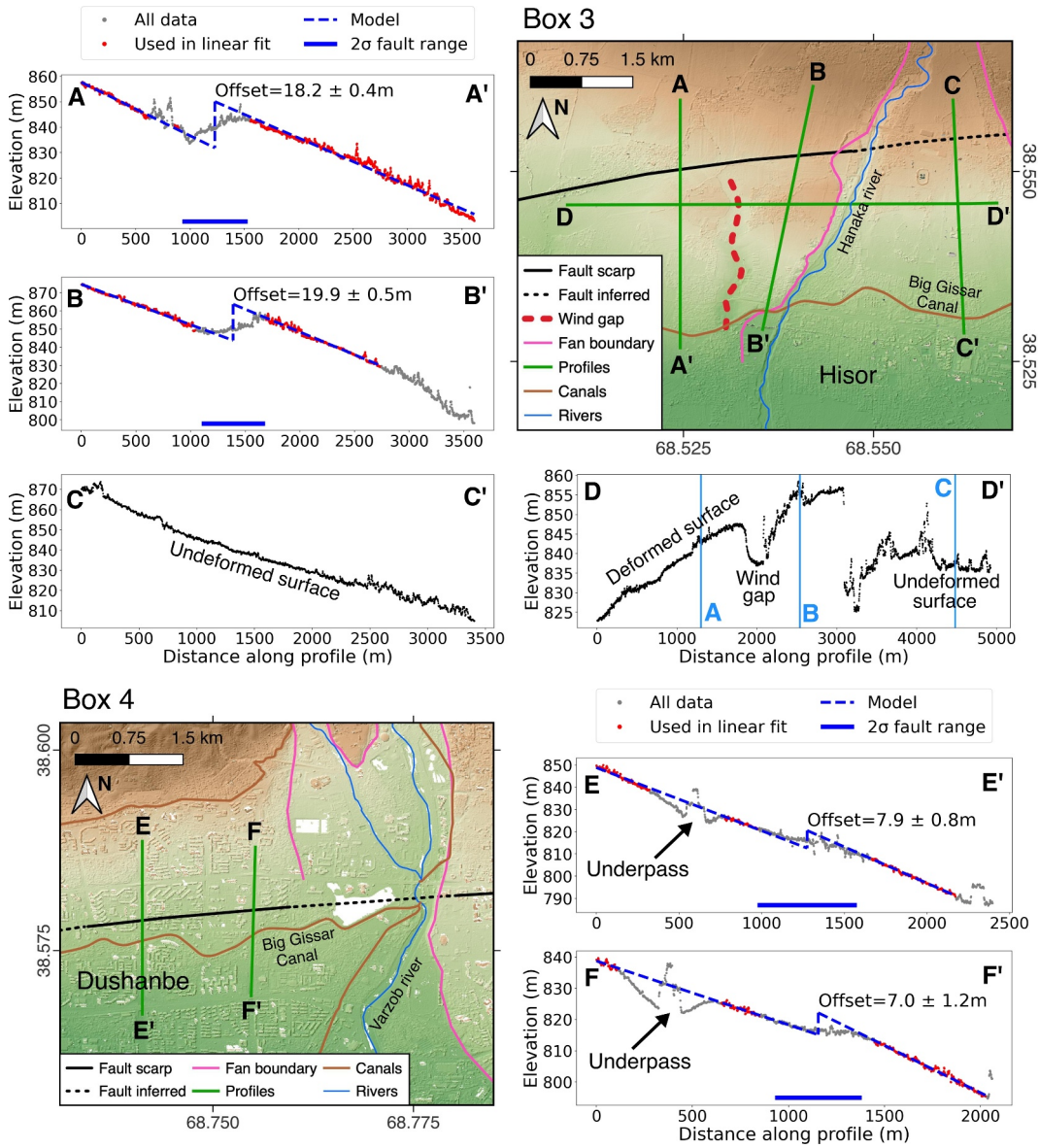

Figure 13. Scarp geomorphology and profiles in Hisor and Dushanbe from Pléiades-derived DEM, corresponding to boxes 3 and 4 in Figure 8. Rivers and canals from OpenStreetMap contributors (2023). Offsets are quoted with their $\pm 1\sigma$ formal uncertainties (Text S3 in Supporting Information S1).

other velocity profiles, and it occurs at the transition between the Quaternary trough sediments and the Neogene hills. Therefore, we are uncertain whether this is truly a tectonic signal or whether it might relate to other processes such as compaction of the Neogene sediments or water extraction. Alternatively, thrust faults within the Dushanbe Trough may be completely locked during the observation period and produce no localized surface displacements.

4.5. Localized Surface Processes

A high-pass filtering of the velocity maps reveals additional surface processes (Figures 5, 14, and 15; Metzger et al., 2021). As first observed by Metzger et al. (2021), aspect-dependent velocities are apparent on the anticlinal ridges of the Tajik Basin: the east- and west-facing slopes of the approximately N-S oriented ridges are moving to the east and west, respectively (Figures 5 and 14). This divergence along ridge crests is likely caused by superficial soil creep or soil slides occurring on talus cones or debris-mantled slopes. Using our high-resolution

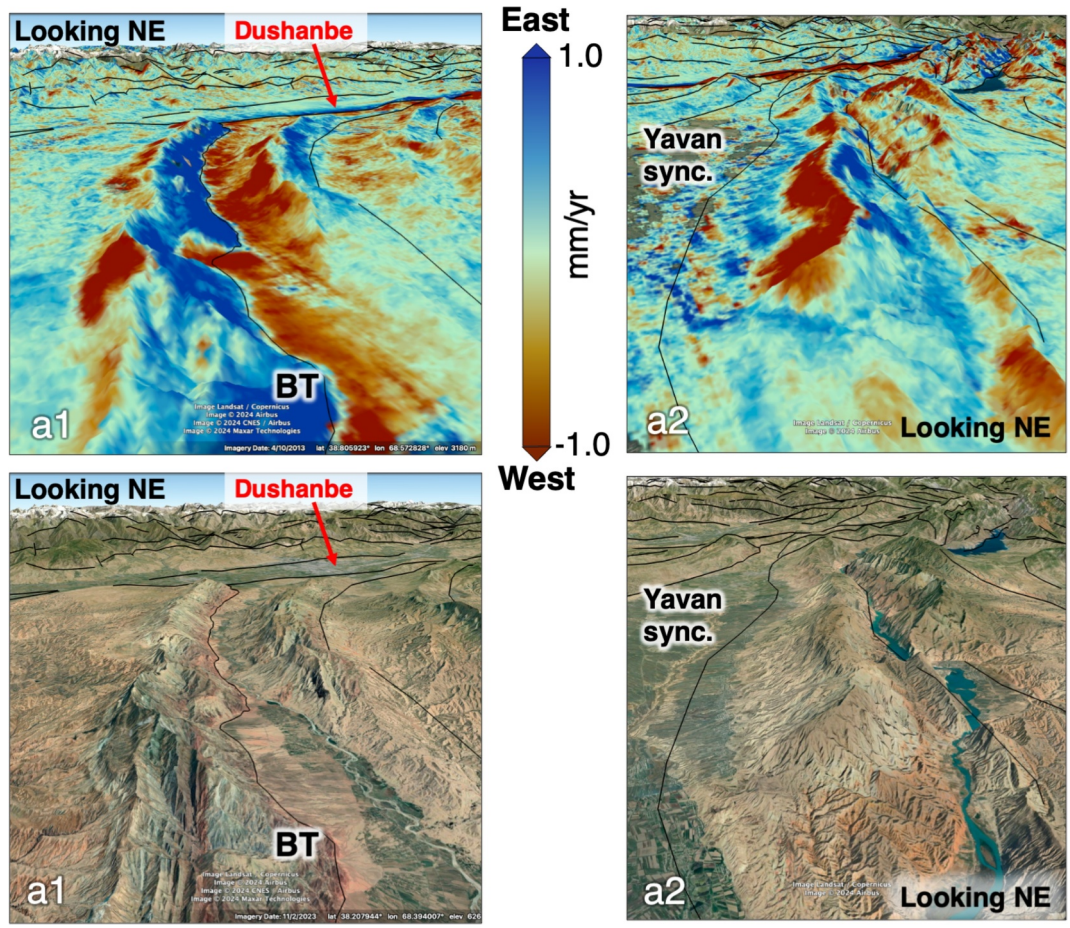

Figure 14. Upper: High-pass filtered eastward velocity maps of areas a1 (left) and a2 (right) in Figure 5 overlain on Google Earth terrain model at 2 x exaggeration showing elongated velocity gradients associated with soil creep or slides occurring on debris mantled slopes. Lower: Google Earth imagery for a1 at eye altitude 11.11 km (left; Land/Copernicus/Airbus/CNES/ Maxar Technologies) and a2 at eye altitude 13.07 km (right; Landsat/Copernicus) with terrain at 2 x exaggeration. Black lines are faults and folds after Dedow et al. (2020) and Abdulhameed et al. (2020).

filtered velocity maps and based on geomorphological characteristics, we also identify rock slope instabilities, as some ridges exhibit higher gradients of velocities concentrated below landslide scarps (Figures 5 and 15). All the mass movements we are able to capture with the intrinsic limitations of InSAR are classified as extremely slow (velocity <16 mm/yr) according to the Landslide Velocity Scale (Cruden & Varnes, 1996). While soil creep might not be hazardous, deep-seated slow-moving landslides involve diverse depths of sliding and a wide range of deformation rates, unsteady or complex behavior, with potentially successive displacements associated with different forcing. Their acceleration or catastrophic failure could be triggered by earthquakes and changes in pore fluid pressure from heavy rainfall, among other forcings, causing damage to housing and infrastructure and potentially also loss of life (Lacroix et al., 2020). It should be noted that the velocities of the extremely slow-moving landslides likely vary in time according to seasonal climatic conditions and other factors (Lacroix et al., 2020), so the measurements from our linear velocity maps represent their average velocities.

Hill slopes with higher horizontal velocity gradients and geomorphological evidence of slope movements include the Kafirnigan River valley near the BT (a1 in Figure 5) and the ridge directly to the east of the Yavan Syncline (a2 in Figure 5). Further detail for these two examples is shown in Figure 14. Towns and villages line the base of these slopes and could be exposed to high risk if these extremely slow-moving landslides evolve into rapid catastrophic landslides. The steep-sloped north-east striking valley in the north-eastern corner of the basin also has higher rates in the filtered eastward velocity map, upstream of the major Nurek Reservoir on either side of the Vashkh River (a3 in Figure 5).

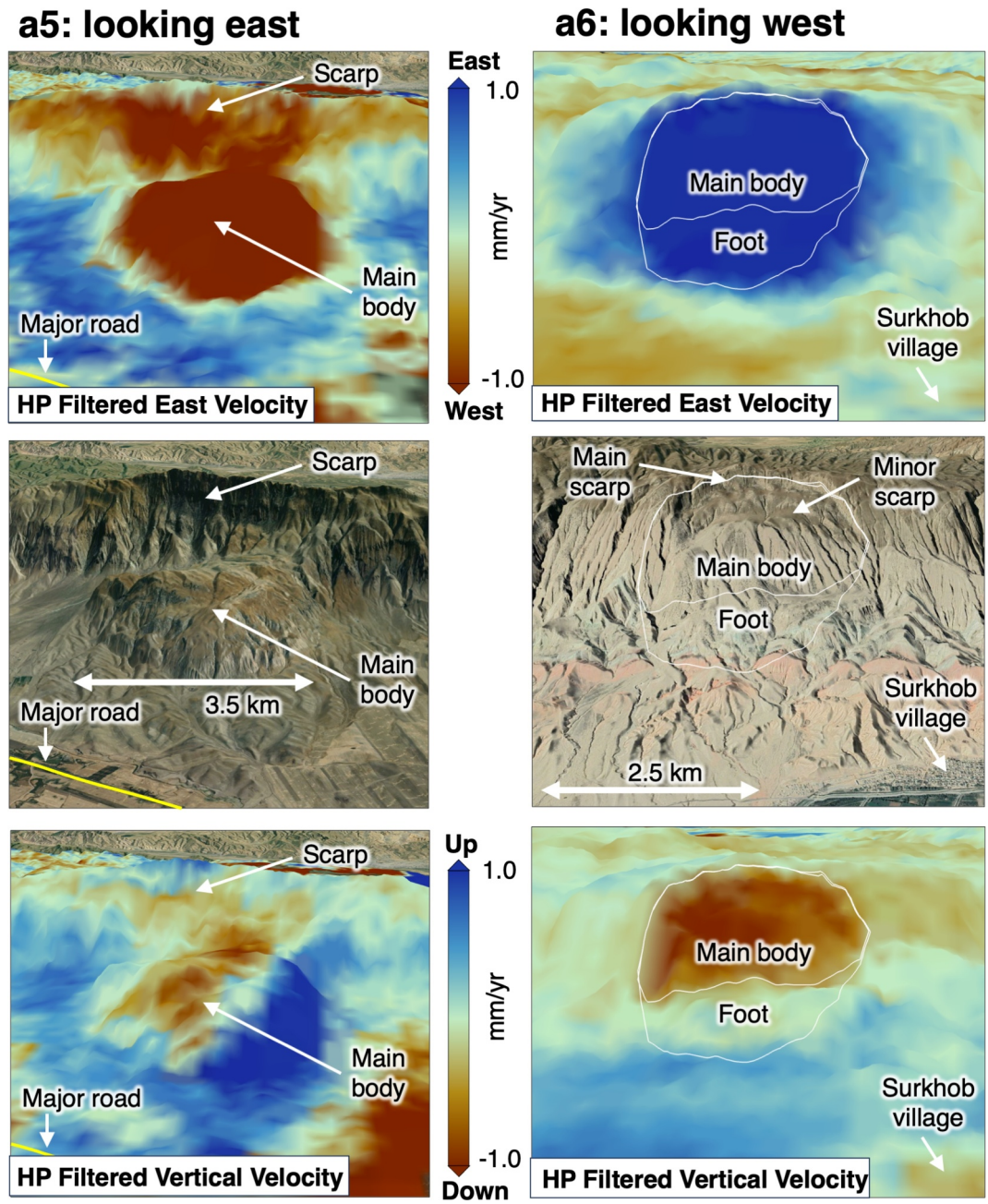

Figure 15. Large rock-slope instabilities at locations a5 (left) and a6 (right) in Figure 5. a5 is located ~5 km south of Dzharteppa village and above the A385, and a6 is above Surkhob village. Upper and lower panels show the high-pass filtered east and vertical velocity maps draped over Google Earth terrain model at 2 x exaggeration. Middle panel is Google Earth Imagery. a5 imagery is Landsat/Copernicus/CNES/Maxar Technologies/Airbus, viewed at 4.29 km eye altitude. a6 imagery is Airbus/CNES/Landsat/Copernicus/Maxar Technologies, viewed at 3.83 km eye altitude.

The extremely slow-moving Baipaza landslide is apparent at location a4 (Figure 5; Figure S19, Table S1 in Supporting Information S1), where a ~5 km wide patch of the east-facing slope is moving eastward at up to ~7 mm/yr, and subsiding by up to ~4 mm/yr. Situated on the west bank of the Vakhsh River, this landslide has shown accelerated movement in the past (1968, 1992, and 2002), leading to partial blockage of the water flow (Havenith et al., 2011, 2018). Reinforcements of the slopes were made in the years following the 2002 failure (Emergency Baipaza Landslide Stabilization Project, 2006). Catastrophic failure of this landslide could impact

the river's flow with possible knock-on effects on the Baipaza HPP (Hydroelectric Power Plant) dam upstream, and the Sangtuda-1 and Sangtuda-2 HPPs infrastructures downstream (Figure 5).

At location a5 (~5 km south of Dzharteppa village; Figures 5; Figure 15; Table S1 in Supporting Information S1), a slow-moving block made of debris detached from the ridge, lies directly above a major road (A385) and a small settlement. This large, rounded, and presumably unconsolidated mass of about ~3 km in diameter is moving up to ~5 mm/yr horizontally. It is subsiding by up to ~1.5 mm/yr on its northern side, whilst the southern side appears to be uplifting and, therefore, accumulating material at up to ~2 mm/yr. Westwards velocity and subsidence are also apparent below the main scarp, suggesting that this deep-seated mountain slope deformation is still active. These velocity patterns might also suggest a rotational sliding of the whole landslide body.

At location a6 (Figures 5 and 15; Table S1 in Supporting Information S1) another landslide scarp is evident in the geomorphology, where a ~3 km wide landslide body on the east-facing slope is moving by up to ~3 mm/yr eastward and subsiding by up to ~2 mm/yr compared to the surrounding sediment. Secondary scarps and active debris flow channels within the main body also indicate that this large rock-slope instability is active. It is located above the village of Surkhob and might pose a hazard to the local population in case of deep-seated slope deformations.

Within the Tajik Gissar, the high-pass filtered velocity maps also reveal down-slope mass movements within some of the valleys with east- and west-facing slopes. In particular, elevated velocities are apparent in the populated Karatag River valley near Shirkent National Park (a7 in Figure 5; Figure S20, Table S1 in Supporting Information S1), and in a small valley ~5 km south of the village of Romit (a8 in Figure 5; Figure S21, Table S1 in Supporting Information S1). Outside of these river valleys, most of the slopes of the southern Tajik Gissar are approximately south-facing, meaning that the InSAR technique is largely insensitive to the horizontal component of their down-slope mass movements, precluding precise landslide mapping to the north of Dushanbe.

Hydrological signals dominate the high-pass filtered vertical velocity map, with vertical motions in agricultural areas related to irrigation and water mass movements (b1 to b6 in Figure 5). The filtered vertical and horizontal maps reveal subsiding patches and aspect-dependent horizontal movements on the low-lying slopes to the north of Dushanbe city (b4 in Figure 5), which indicate superficial creep. We note that river channels in the Yavan Syncline (b5 in Figure 5) and the Kyzylsu River Valley (b6 in Figure 5) at the eastern edge of the map exhibit uplift signals. This uplift could result from slow sediment aggradation—slow enough to preserve InSAR coherence—that outpaces channel erosion over the 2014–2021 period. Alternatively, it may reflect hydrological effects, such as a rise in the groundwater table between 2014 and 2021.

5. Discussion

Our bespoke processing approach produced InSAR rate maps with a higher spatial resolution and more continuous coverage than published geodetic data sets (Ischuk et al., 2013; Metzger et al., 2020, 2021; Mohadjer et al., 2010; Zubovich et al., 2010), allowing us to map and quantify the deformation in our study area in more detail than was previously possible. We have shown that the IF, which passes through the south of Dushanbe city, creeps to very shallow depths (~0–700 m) at a rate of ~4–9 mm/yr, decreasing east to west as slip is transferred onto basin thrusts. Our results are consistent with Metzger et al. (2021) who estimated similar rates (~5–10 mm/yr) and suggested the locking depth was likely to be at most 1 km, based on lower resolution rate maps. The aseismic slip probably extends to around ~4–6 km depth, as this is the approximate thickness of the basin sediments along the IF, according to a seismic section interpreted by Gągała et al. (2020). An Upper Jurassic evaporite-bearing unit occurs near the base of the sedimentary sequence, and rocks of this age crop out at the surface along parts of the IF trace (Gągała et al., 2020). As such, the creeping behavior of the IF and also of thrust sheets within the Tajik Basin to the south appear to be controlled by the presence of the evaporitic layer. It is important to note that for large stretches of the IF there is little to no geomorphic indication of recent slip. Our high-resolution InSAR approach hence reveals new information on the location of the fault trace, how the fault terminates, and the partitioning of slip onto secondary structures. We image the westward transfer of right-lateral slip onto a series of thrusts and folds within the Tajik Basin, with at least one of these thrusts, the BT, creeping to the surface.

It is unlikely that the shallow creeping parts of the IF pose a significant seismic hazard to Dushanbe, if the creep occurs at the full long-term slip-rate, and if it represents its long-term stable behavior. However,

earthquake catalogues show events of up to $M_L \sim 5.5$ at ∼4–17 km depth beneath the surface trace of the IF, with available focal mechanisms consistent with right-lateral strike-slip (Djuraev & Shakirdzanova, 1993; Kufner et al., 2018), indicating the presence of a seismogenic fault within the basement beneath the evaporite detachment layer (Figure 2). We do not observe any longer wavelength signals in our eastward velocity map indicative of locking and strain accumulation at depth. This may mean that the slip-rate on the basement fault is significantly slower than that on the upper part of the fault, or the absence of a longer wavelength signal may be a result of the decoupling of the sedimentary cover from the basement to the south of the IF. Therefore, there is a hazard from the fault at depth which cannot be mapped or measured using surface velocity data. This highlights the need to consider a range of data sets when identifying sources of seismic hazard, and the limitations of surface velocity measurements in regions with mechanical decoupling of basement from surficial deposits.

Through our remote geomorphic mapping, we also document recent activity on the DT, a south-dipping thrust fault, which we map for ∼45 km through the Dushanbe Trough. Whilst we found ∼1 mm/yr of possible uplift in one of the surface velocity profiles across the western end of this fault, we were unable to confidently confirm a tectonic origin for the signal. The absence of an observed surface velocity gradient across this E-W striking fault is not inconsistent with the fault being active, as much of the deformation is likely to be in the N-S direction, to which the InSAR technique is largely insensitive (Elliott et al., 2016), and the thrust may be fully locked during the observation period. We cannot be certain whether the DT is slipping aseismically along an evaporite horizon or whether it may produce earthquakes. However, in contrast to the main part of the Tajik basin, borehole data show that the Gaurdak formation is either absent or much thinner in the Dushanbe Trough, and there is no clear evidence for evaporites (Gągała et al., 2020; Leith, 1985). Furthermore, according to interpretations of seismic reflection profiles and borehole data by Gągała et al. (2020), in contrast to the decoupling to the south of the IF, within the Dushanbe Trough, faults and folds deform the basement and sedimentary cover together as one mechanical layer. Therefore, without an evaporite horizon on which to slip aseismically and with no evidence of decoupling, it is possible that the DT is locked and could produce seismic ruptures that extend into the basement. With its proximity to the city, even a small earthquake on this fault could be destructive. There is therefore an urgent need for field studies, such as paleoseismic trenching, to better constrain the seismogenic potential of the Dushanbe Trough and the level of connectivity of remotely mapped scarps.

By applying a high-pass filter to our InSAR maps we reveal widespread soil creep, confirming the divergence along ridge crests first identified by Metzger et al. (2021), as well as identifying localized slope instabilities at several locations across the Tajik Basin. Some of these slow-moving landslides are located above settlements, roads, or dammed rivers in the Tajik Basin and Tajik Gissar. These moving masses could potentially damage or impact infrastructure (including hydroelectric power plants) or block access routes to the mountains if they failed catastrophically (e.g., in response to earthquake shaking). Soil creep or slide along the northern slopes of the Dushanbe basin might represent additional landslide hazards in proximity to Dushanbe, but our data is not optimal for imaging movement on south-facing slopes as the InSAR technique has low sensitivity to N-S directed motion.

6. Conclusion

Using Multi-Temporal InSAR, we show the westwards movement of the Tajik Basin relative to its surroundings, with deformation concentrated on the Ilyak fault to the north and the Babatag thrust to the west, both of which are slipping aseismically or creeping along an evaporite-bearing horizon. The detailed information from our high-resolution data set enables us to map and quantify short-wavelength deformation on individual faults, including creep, as well as downslope movements affecting hillslopes composed of poorly consolidated sediments. We document shallow right-lateral aseismic slip on the Ilyak fault, with a slip rate of ∼9 mm/yr at its eastern end, decreasing to ∼4 mm/yr in the west, due to a transfer of dextral slip to the fold and thrust belt of the Tajik Basin. Though the major surficial faults are shown to be creeping, seismicity indicates that a locked fault does exist at depth beneath the Ilyak fault, posing a hazard to Dushanbe. We find additional geomorphic evidence for slip on a south-dipping thrust fault within the Dushanbe Trough, which runs through Dushanbe city and we suggest could potentially be a source of seismic hazard. Field investigations of this Dushanbe Trough thrust are needed to determine its seismogenic potential. Finally, we map several rock slope instabilities and soil creep, which could pose a hazard to communities and infrastructure if they accelerate and detach in response to seismic shaking or precipitation.

Conflict of Interest

The authors declare no conflicts of interest relevant to this study.

Data Availability Statement

The new data sets presented in this study have been made available online: velocity maps are preserved in Wilkinson et al. (2025) and point clouds of the digital elevation data are preserved in Wilkinson and Walker (2025). The InSAR analysis uses Copernicus Sentinel-1 data [2014–2021], freely available from the Copernicus Data Space Ecosystem (https://dataspace.copernicus.eu/). Atmospheric corrections to interferograms were generated using the free ECMWF ERA-5 atmospheric model from the Copernicus Climate Change Service (Hersbach et al., 2020). Neither the European Commission nor ECMWF is responsible for any use that may be made of the Copernicus information or data it contains. Some maps were prepared using GMT (Wessel et al., 2019) or PyGMT (Tian et al., 2025). Some map data are from OpenStreetMap contributors (2023) and copyrighted OpenStreetMap contributors, licensed under the Open Database License (https://www.openstreetmap.org/copyright), and freely available from https://www.openstreetmap.org.

Acknowledgments

We thank Sanaa Reuter (née Abdulhameed) for kindly sharing the shapefiles of the geological mapping from Abdulhameed et al. (2020) and Gągała et al. (2020). Thanks also to Barry Parsons for his advice on the direction of the research, to Aidyn Mukambayev for sharing local earthquake catalogues, to Maria Petrunova for translating them into English, to Tom Garth for his advice on interpreting earthquake catalogues, and to Alex Lipp for discussions about the best approaches to statistics. *We are grateful to S. Metzger and Z. Çakır for their thorough reviews. We also thank Ekbal Hussain and Robert Hilton who gave helpful comments on this project as PhD thesis examiners.* This research is supported by the UK National Environment Research Council (NERC; Doctoral Training Partnership in Environmental Research; NE/L002612/1 and NE/S007474/1), the NERC-funded Centre for Observation and Modelling of Earthquakes, Volcanoes and Tectonics (COMET; GA/13/M/031), the NERC grant "Looking into the Continents from Space" (LiCS; NE/K011006/1), and the NERC-ESRC Increasing Resilience to Natural Hazards program "Earthquakes without Frontiers (EwF)" (NE/J02001X/1). Additionally, this work is supported by the Leverhulme Trust Research Project Grant "EROICA" (RPG-2018-371). Four pairs of Pleiades satellite stereo images were obtained at no cost through the Committee for Earth Observing Satellites (CEOS) Seismic Hazard Demonstrator. The other four pairs were bought (in 2020) using the St Edmund Hall Potanin Research Fund.

References

Abdulhameed, S., Ratschbacher, L., Jonckheere, R., Gągała, Ł., Enkelmann, E., Käßner, A., et al. (2020). Tajik basin and southwestern Tian Shan, northwestern India-Asia collision zone: 2. Timing of basin inversion, Tian Shan mountain building, and relation to Pamir-Plateau advance and deep India-Asia indentation. *Tectonics*, *39*(5), e2019TC005873. https://doi.org/10.1029/2019TC005873

Ansari, H., De Zan, F., & Parizzi, A. (2021). Study of systematic bias in measuring surface deformation with SAR interferometry. *IEEE Transactions on Geoscience and Remote Sensing*, *59*(2), 1285–1301. https://doi.org/10.1109/TGRS.2020.3003421

Avouac, J. P., & Burov, E. B. (1996). Erosion as a driving mechanism of intracontinental mountain growth. *Journal of Geophysical Research*, *101*(B8), 17747–17769. https://doi.org/10.1029/96JB01344

Bamler, R., & Hartl, P. (1998). Synthetic aperture radar interferometry. *Inverse Problems*, *14*(4), R1–R54. https://doi.org/10.1088/0266-5611/14/4/001

Bindi, D., Parolai, S., Gómez-Capera, A., Locati, M., Kalmetyeva, Z., & Mikhailova, N. (2014). Locations and magnitudes of earthquakes in Central Asia from seismic intensity data. *Journal of Seismology*, *18*(1), 1–21. https://doi.org/10.1007/s10950-013-9392-1

Bourgeois, O., Cobbold, P. R., Rouby, D., Thomas, J. C., & Shein, V. (1997). Least squares restoration of Tertiary thrust sheets in map view, Tajik depression, Central Asia. *Journal of Geophysical Research*, *102*(B12), 27553–27573. https://doi.org/10.1029/97JB02477

Bullen, M., Burbank, D., Garver, J., & Abdrakhmatov, K. (2001). Late Cenozoic tectonic evolution of the northwestern Tien Shan: New age estimates for the initiation of mountain building. *Geological Society of America Bulletin*, *113*(12), 1544–1559. https://doi.org/10.1130/0016-7606(2001)113<1544:LCTEOT>2.0.CO;2

Chen, W.-P., & Molnar, P. (1977). Seismic moments of major earthquakes and the average rate of slip in Central Asia. *Journal of Geophysical Research*, *82*(20), 2945–2969. https://doi.org/10.1029/JB082i020p02945

Cruden, D., & Varnes, D. (1996). Landslide types and processes. In A. K. Turner & R. L. Schuster (Eds.), *Landslides: Investigation and mitigation* (Vol. 247, pp. 37–75). Transportation Research Board. Retrieved from https://trid.trb.org/view/462501

Daout, S., D'Agostino, N., Pathier, E., Socquet, A., Lavé, J., Doin, M.-P., et al. (2023). Along-strike variation of the strain partitioning within the Apenines as seen from large-scale multi-temporal InSAR analysis. *Tectonophysics*, *867*, 230076. https://doi.org/10.1016/j.tecto.2023.230076

Daout, S., Dini, B., Haeberli, W., Doin, M.-P., & Parsons, B. (2020). Ice loss in the northeastern Tibetan Plateau permafrost as seen by 16 yr of ESA SAR missions. *Earth and Planetary Science Letters*, *545*, 116404. https://doi.org/10.1016/j.epsl.2020.116404

Daout, S., Doin, M. P., Peltzer, G., Socquet, A., & Lasserre, C. (2017). Large-scale InSAR monitoring of permafrost freeze-thaw cycles on the Tibetan Plateau. *Geophysical Research Letters*, *44*(2), 901–909. https://doi.org/10.1002/2016GL070781

Daout, S., Sudhaus, H., Kausch, T., Steinberg, A., & Dini, B. (2019). Interseismic and postseismic shallow creep of the north Qaidam thrust faults detected with a multitemporal InSAR analysis. *Journal of Geophysical Research: Solid Earth*, *124*(7), 7259–7279. https://doi.org/10.1029/2019JB017692

Dedow, R., Franz, M., Szulc, A., Schneider, J. W., Brückner, J., Ratschbacher, L., et al. (2020). Tajik Basin and southwestern Tian Shan, northwestern India-Asia collision zone: 3. Preorogenic to synorogenic retro-foreland basin evolution in the eastern Tajik Depression and linkage to the Pamir hinterland. *Tectonics*, *39*(5), e2019TC005874. https://doi.org/10.1029/2019TC005874

De Luca, C., Casu, F., Manunta, M., Onorato, G., & Lanari, R. (2022). Comments on "Study of systematic bias in measuring surface deformation with SAR interferometry". *IEEE Transactions on Geoscience and Remote Sensing*, *60*, 1–5. https://doi.org/10.1109/TGRS.2021.3103037

De Zan, F., Parizzi, A., Prats-Iraola, P., & Lopez-Dekker, P. (2014). A SAR interferometric model for soil moisture. *IEEE Transactions on Geoscience and Remote Sensing*, *52*(1), 418–425. https://doi.org/10.1109/TGRS.2013.2241069

Djuraev, R., & Shakirdzanova, G. (1993). The Gissar earthquake 22.01.1989. In *Earthquakes in the USSR in 1989* (pp. 76–84). Nauka. (in Russian).

Dodds, N., Daout, S., Walker, R. T., Begenjev, G., Bezmenov, Y., Mirzin, R., & Parsons, B. (2022). Interseismic deformation and strain-partitioning along the Main Köpetdag Fault, Turkmenistan, with Sentinel-1 InSAR time-series. *Geophysical Journal International*, *230*(3), 1612–1629. https://doi.org/10.1093/gji/ggac139

Doin, M.-P., Lasserre, C., Peltzer, G., Cavalié, O., & Doubre, C. (2009). Corrections of stratified tropospheric delays in SAR interferometry: Validation with global atmospheric models. *Journal of Applied Geophysics*, *69*(1), 35–50. https://doi.org/10.1016/j.jappgeo.2009.03.010

Doin, M.-P., Lodge, F., Guillaso, S., Jolivet, R., Lasserre, C., Ducret, G., et al. (2011). Presentation of the small baseline NSBAS processing chain on a case example: The Etna deformation monitoring from 2003 to 2010 using Envisat data. In *Proceedings of fringe 2011: Advances in the science and applications of SAR interferometry* (Vol. SP-697). European Space Agency.

Doin, M.-P., Twardzik, C., Ducret, G., Lasserre, C., Guillaso, S., & Jianbao, S. (2015). InSAR measurement of the deformation around Siling Co Lake: Inferences on the lower crust viscosity in central Tibet. *Journal of Geophysical Research: Solid Earth*, *120*(7), 5290–5310. https://doi.org/10.1002/2014JB011768

Elliott, J., Walters, R., & Wright, T. (2016). The role of space-based observation in understanding and responding to active tectonics and earthquakes. *Nature Communications*, *7*(1), 13844. https://doi.org/10.1038/ncomms13844

Emergency Baipaza Landslide Stabilization Project (Tech. Rep.). (2006). Asian development bank. Retrieved from https://www.adb.org/projects/documents/tajikistan-36233-013

Engdahl, E. R., Di Giacomo, D., Sakarya, B., Gkarlaouni, C. G., Harris, J., & Storchak, D. A. (2020). ISC-EHB 1964–2016, an improved data set for studies of earth structure and global seismicity. *Earth and Space Science*, *7*(1), e2019EA000897. https://doi.org/10.1029/2019EA000897

Engdahl, R., Van Der Hilst, R., & Buland, R. (1998). Global teleseismic earthquake relocation with improved travel times and procedures for depth determination. *Bulletin of the Seismological Society of America*, *88*(3), 722–743. https://doi.org/10.1785/bssa0880030722

Evans, S. G., Roberts, N. J., Ischuk, A., Delaney, K. B., Morozova, G. S., & Tutubalina, O. (2009). Landslides triggered by the 1949 Khait earthquake, Tajikistan, and associated loss of life. *Engineering Geology*, *109*(3–4), 195–212. https://doi.org/10.1016/j.enggeo.2009.08.007

Funning, G. J. (2005). Source parameters of large shallow earthquakes in the Alpine-Himalayan belt from InSAR and waveform modelling (Ph.D. Thesis). Retrieved from https://solo.bodleian.ox.ac.uk/permalink/f/89vilt/oxfaleph016632892

Gągała, Ł., Ratschbacher, L., Ringenbach, J., Kufner, S., Schurr, B., Dedow, R., et al. (2020). Tajik Basin and southwestern Tian Shan, northwestern India-Asia collision zone: 1. Structure, kinematics, and salt tectonics in the Tajik fold-and-thrust belt of the western foreland of the Pamir. *Tectonics*, *39*(5), e2019TC005871. https://doi.org/10.1029/2019TC005871

Grandin, R. (2015). Interferometric processing of SLC sentinel-1 TOPS data. In *Proceedings of fringe 2015: Advances in the science and applications of SAR interferometry and sentinel-1 InSAR workshop* (Vol. SP-731). European Space Agency. https://doi.org/10.5270/Fringe2015.pp116

Grandin, R., Doin, M.-P., Bollinger, L., Pinel-Puysségur, B., Ducret, G., Jolivet, R., & Sapkota, S. N. (2012). Long-term growth of the Himalaya inferred from interseismic InSAR measurement. *Geology*, *40*(12), 1059–1062. https://doi.org/10.1130/G33154.1

Havenith, H.-B., Abdrakhmatov, K., Torgoev, I., Ischuk, A., Strom, A., Bystricky, E., & Cipciar, A. (2011). Earthquakes, landslides, dams and reservoirs in the Tian Shan, Central Asia. In *Proceedings of the second world landslide forum* (pp. 3/10–7/10). Alexander Strom.

Havenith, H.-B., Torgoev, I., & Ischuk, A. (2018). Integrated geophysical-geological 3D model of the right-bank slope downstream from the Rogun Dam construction site, Tajikistan. *International Journal of Geophysics*, *2018*(1), 1641789. https://doi.org/10.1155/2018/1641789

Hersbach, H., Bell, B., Berrisford, P., Hirahara, S., Horányi, A., Muñoz-Sabater, J., et al. (2020). The ERA5 global reanalysis. *Quarterly Journal of the Royal Meteorological Society*, *146*(730), 1999–2049. https://doi.org/10.1002/qj.3803

International Seismological Centre. (2022). On-line bulletin [Dataset]. https://doi.org/10.31905/D808B830

International Seismological Centre. (2025). On-line bulletin [Dataset]. https://doi.org/10.31905/D808B830

Ischuk, A., Bendick, R., Rybin, A., Molnar, P., Khan, S. F., Kuzikov, S., et al. (2013). Kinematics of the Pamir and Hindu Kush regions from GPS geodesy. *Journal of Geophysical Research: Solid Earth*, *118*(5), 2408–2416. https://doi.org/10.1002/jgrb.50185

Ishihara, K., Okusa, S., Oyagi, N., & Ischuk, A. (1990). Liquefaction-induced flow slide in the collapsible loess deposit in Soviet Tajik. *Soils and Foundations*, *28*(5), 282. https://doi.org/10.1016/0148-9062(91)90223-9

Jolivet, R., Grandin, R., Lasserre, C., Doin, M.-P., & Peltzer, G. (2011). Systematic InSAR tropospheric phase delay corrections from global meteorological reanalysis data. *Geophysical Research Letters*, *38*(17). https://doi.org/10.1029/2011GL048757

Kalmetieva, Z., Mikolaichuk, A., Moldobekov, B., Meleshko, A., Jantaev, M., & Zubovich, A. (2009). Atlas of earthquakes in Kyrgyzstan. Retrieved from https://www.caiag.kg/en/projects/114-atlas-zemletryasenij-kyrgyzstana

Kondorskaya, N., Shebalin, N., Khrometskaya, Y. A., & Gvishiani, A. (Eds.) (1982)., *New catalog of strong earthquakes in the U.S.S.R. from ancient times through 1977*. World Data Center A for Solid Earth Geophysics.

Kufner, S.-K., Kakar, N., Bezada, M., Bloch, W., Metzger, S., Yuan, X., et al. (2021). The Hindu Kush slab break-off as revealed by deep structure and crustal deformation. *Nature Communications*, *12*(1), 1685. https://doi.org/10.1038/s41467-021-21760-w

Kufner, S.-K., Schurr, B., Ratschbacher, L., Murodkulov, S., Abdulhameed, S., Ischuk, A., et al. (2018). Seismotectonics of the Tajik Basin and surrounding mountain ranges. *Tectonics*, *37*(8), 2404–2424. https://doi.org/10.1029/2017TC004812

Kulikova, G. (2016). Source parameters of the major historical earthquakes in the Tien-Shan region from the late 19th to the early 20th century (Ph.D. Thesis). Retrieved from http://nbn-resolving.de/urn:nbn:de:kobv:517-opus4-88370

Lacroix, P., Handwerger, A. L., & Bièvre, G. (2020). Life and death of slow-moving landslides. *Nature Reviews Earth & Environment*, *1*(8), 404–419. https://doi.org/10.1038/s43017-020-0072-8

Lazear, G., Karlstrom, K., Aslan, A., & Kelley, S. (2013). Denudation and flexural isostatic response of the Colorado Plateau and southern Rocky Mountains region since 10 Ma. *Geosphere*, *9*(4), 792–814. https://doi.org/10.1130/GES00836.1

Leith, W. (1985). A mid-Mesozoic extension across Central Asia? *Nature*, *313*(6003), 567–570. https://doi.org/10.1038/313567a0

Leith, W., & Alvarez, W. (1985). Structure of the Vakhsh fold-and-thrust belt Tadjik SSR: Geologic mapping on a Landsat image base. *Geological Society of America Bulletin*, *96*(7), 875–885. https://doi.org/10.1130/0016-7606(1985)96<875:SOTVFB>2.0.CO;2

Lemrabet, L., Doin, M.-P., Lasserre, C., & Durand, P. (2023). Referencing of continental-scale InSAR-derived velocity fields: Case study of the eastern Tibetan Plateau. *Journal of Geophysical Research: Solid Earth*, *128*(7), e2022JB026251. https://doi.org/10.1029/2022JB026251

Liu, S., & Jónsson, S. (2025). Glacial isostatic uplift in the Tibetan Plateau and surroundings. *Geophysical Research Letters*, *52*(13), e2025GL114899. https://doi.org/10.1029/2025GL114899

López-Quiroz, P., Doin, M.-P., Tupin, F., Briole, P., & Nicolas, J.-M. (2009). Time series analysis of Mexico City subsidence constrained by radar interferometry. *Journal of Applied Geophysics*, *69*(1), 1–15. https://doi.org/10.1016/j.jappgeo.2009.02.006

Maghsoudi, Y., Hooper, A. J., Wright, T. J., Lazecky, M., & Ansari, H. (2022). Characterizing and correcting phase biases in short-term, multilooked interferograms. *Remote Sensing of Environment*, *275*, 113022. https://doi.org/10.1016/j.rse.2022.113022

Mathey, M., Doin, M., André, P., Walpersdorf, A., Baize, S., & Sue, C. (2022). Spatial heterogeneity of uplift pattern in the western European Alps revealed by InSAR time-series analysis. *Geophysical Research Letters*, *49*(1), e2021GL095744. https://doi.org/10.1029/2021GL095744

McNab, F., Sloan, R. A., & Walker, R. T. (2019). Simultaneous orthogonal shortening in the Afghan-Tajik Depression. *Geology*, *47*(9), 862–866. https://doi.org/10.1130/G46090.1

Metzger, S., Gągała, Ł., Ratschbacher, L., Lazecký, M., Maghsoudi, Y., & Schurr, B. (2021). Tajik Depression and Greater Pamir neotectonics from InSAR rate maps. *Journal of Geophysical Research: Solid Earth*, *126*(12), e2021JB022775. https://doi.org/10.1029/2021JB022775

Metzger, S., Ischuk, A., Deng, Z., Ratschbacher, L., Perry, M., Kufner, S., et al. (2020). Dense GNSS profiles across the northwestern tip of the India-Asia collision zone: Triggered slip and westward flow of the Peter the First Range Pamir, into the Tajik Depression, *39*(2), e2019TC005797. https://doi.org/10.1029/2019TC005797

Mikhailova, N., Poleshko, N., Aristova, I., Mukambayev, A., & Kulikova, G. (2015). EMCA Central Asia earthquake catalogue v1.1 [Dataset]. *GFZ Data Services*. https://doi.org/10.5880/GFZ.EWS.2015.001

Mohadjer, S., Bendick, R., Ischuk, A., Kuzikov, S., Kostuk, A., Saydullaev, U., et al. (2010). Partitioning of India-Eurasia convergence in the Pamir-Hindu Kush from GPS measurements. *Geophysical Research Letters*, *37*(4). https://doi.org/10.1029/2009GL041737

Nikonov, A. A., & Shebalina, T. Y. (1979). Lichenometry and earthquake age determination in Central Asia. *Nature*, *280*(5724), 675–677. https://doi.org/10.1038/280675a0

OpenStreetMap contributors. (2023). OpenStreetMap [Dataset]. Retrieved from https://www.openstreetmap.org

Pilz, M., Bindi, D., Boxberger, T., Hakimov, F., Moldobekov, B., Murodkulov, S., et al. (2013). First steps toward a reassessment of the seismic risk of the city of Dushanbe (Tajikistan). *Seismological Research Letters*, *84*(6), 1026–1038. https://doi.org/10.1785/0220130040

Pinel-Puyssegur, B., Michel, R., & Avouac, J.-P. (2012). Multi-link InSAR time series: Enhancement of a wrapped interferometric database. *Ieee Journal of Selected Topics in Applied Earth Observations and Remote Sensing*, *5*(3), 784–794. https://doi.org/10.1109/JSTARS.2012.2196758

Robinson, A. C., Yin, A., Manning, C. E., Harrison, T. M., Zhang, S.-H., & Wang, X.-F. (2004). Tectonic evolution of the northeastern Pamir: Constraints from the northern portion of the Cenozoic Kongur Shan extensional system, western China. *Geological Society of America Bulletin*, *116*(7), 953–973. https://doi.org/10.1130/B25375.1

Rosen, P. A., Hensley, S., Peltzer, G., & Simons, M. (2004). Updated repeat orbit interferometry package released. *Eos, Transactions American Geophysical Union*, *85*(5), 47. https://doi.org/10.1029/2004EO050004

Savage, J. C., & Burford, R. O. (1973). Geodetic determination of relative plate motion in central California. *Journal of Geophysical Research*, *78*(5), 832–845. https://doi.org/10.1029/JB078i005p00832

Schurr, B., Ratschbacher, L., Sippl, C., Gloaguen, R., Yuan, X., & Mechie, J. (2014). Seismotectonics of the Pamir. *Tectonics*, *33*(8), 1501–1518. https://doi.org/10.1002/2014TC003576

Shuttle Radar Topography Mission (SRTM) Global. (2013). Open topography [Dataset]. https://doi.org/10.5069/G9445JDF

Sippl, C., Schurr, B., Yuan, X., Mechie, J., Schneider, F. M., Gadoev, M., et al. (2013). Geometry of the Pamir-Hindu Kush intermediate-depth earthquake zone from local seismic data. *Journal of Geophysical Research: Solid Earth*, *118*(4), 1438–1457. https://doi.org/10.1002/JGRB.50128

Statistical Agency under the President of the Republic of Tajikistan. (2022). Population number and distribution: The number of permanent residents in regions, districts, urban areas, district centers and settlements with a population of 5 thousand people or more [in Tajik and Russian] (Tech. Rep.). Retrieved from https://www.stat.tj/wp-content/uploads/2024/05/tablicza-1.-chislennost-postoyannogo-naseleniya-po-oblastyam-rajonam-gorodskim-poseleniyam-rajonnym-czentram-i-selskim-naselennym-punktam-s-chis.pdf

Storchak, D. A., Harris, J., Brown, L., Lieser, K., Shumba, B., & Di Giacomo, D. (2020). Rebuild of the bulletin of the International Seismological Centre (ISC)—Part 2: 1980–2010. *Geoscience Letters*, *7*(1), 1–21. https://doi.org/10.1186/S40562-020-00164-6/FIGURES/16

Strecker, M. R., Frisch, W., Hamburger, M. W., Ratschbacher, L., Semiletkin, S., Zamoruyev, A., & Sturchio, N. (1995). Quaternary deformation in the eastern Pamirs, Tadzhikistan and Kyrgyzstan. *Tectonics*, *14*(5), 1061–1079. https://doi.org/10.1029/95TC00927

Stübner, K., Ratschbacher, L., Rutte, D., Stanek, K., Minaev, V., Wiesinger, M., et al. (2013). The giant Shakhdara migmatitic gneiss dome, Pamir, India-Asia collision zone: 1. Geometry and kinematics. *Tectonics*, *32*(4), 948–979. https://doi.org/10.1002/tect.20057

Tian, D., Uieda, L., Leong, W. J., Fröhlich, Y., Grund, M., Schlitzer, W., et al. (2025). PyGMT: A python interface for the generic mapping tools [Software]. *Zenodo*. https://doi.org/10.5281/ZENODO.3781524

Turcotte, D. L., & Schubert, G. (2014). *Geodynamics* (3rd ed. ed.). Cambridge University Press.

Vernant, P., Hivert, F., Chéry, J., Steer, P., Cattin, R., & Rigo, A. (2013). Erosion-induced isostatic rebound triggers extension in low convergent mountain ranges. *Geology*, *41*(4), 467–470. https://doi.org/10.1130/G33942.1

Wang, D., Zhao, B., Li, J., Metzger, S., Gu, C., Wang, W., et al. (2024). Recent block kinematics and fault slip rates in the Pamir, Central Asia, from an integrated GNSS velocity field. *Tectonics*, *43*(10), e2024TC008475. https://doi.org/10.1029/2024TC008475

Wessel, P., Luis, J. F., Uieda, L., Scharroo, R., Wobbe, F., Smith, W. H. F., & Tian, D. (2019). The generic mapping tools version 6 [Software]. *Geochemistry, Geophysics, Geosystems*, *20*(11), 5556–5564. https://doi.org/10.1029/2019GC008515

Weston, J., Engdahl, E. R., Harris, J., Di Giacomo, D., & Storchak, D. A. (2018). ISC-EHB: Reconstruction of a robust earthquake data set. *Geophysical Journal International*, *214*(1), 474–484. https://doi.org/10.1093/gji/ggy155

Wilkinson, R., Daout, S., & Dodds, N. (2025). MT-InSAR-derived velocity maps of the Tajik Basin and Dushanbe Trough [Dataset]. *Zenodo*. https://doi.org/10.5281/ZENODO.14253864

Wilkinson, R., & Walker, R. (2025). Point clouds of Dushanbe Trough (Tajikistan) elevation derived from Pleiades stereo imagery [Dataset]. *Zenodo*. https://doi.org/10.5281/ZENODO.15911203

Wright, T. J., Parsons, B., England, P. C., & Fielding, E. J. (2004). InSAR observations of low slip rates on the major faults of western Tibet. *Science*, *305*(5681), 236–239. https://doi.org/10.1126/science.1096388

Yin, A., Robinson, A., & Manning, C. E. (2001). *Oroclinal bending and slab-break-off causing coeval east-west extension and east-west contraction in the Pamir-Nanga Parbat Syntaxis in the past 10 M.y*. American Geophysical Union. Retrieved from https://ui.adsabs.harvard.edu/abs/2001AGUFM.T12F..03Y

Zubovich, A. V., Wang, X. Q., Scherba, Y. G., Schelochkov, G. G., Reilinger, R., Reigber, C., et al. (2010). GPS velocity field for the Tien Shan and surrounding regions. *Tectonics*, *29*(6), TC6014. https://doi.org/10.1029/2010TC002772

References From the Supporting Information

Ainscoe, E. A., Abdrakhmatov, K. E., Baikulov, S., Carr, A. S., Elliott, A. J., Grützner, C., & Walker, R. T. (2019). Variability in surface rupture between successive earthquakes on the Suusamyr Fault, Kyrgyz Tien Shan: Implications for palaeoseismology. *Geophysical Journal International*, *216*(1), 703–725. https://doi.org/10.1093/gji/ggy457

Bowman, D. (2019). *Principles of alluvial fan morphology*. Springer Netherlands. https://doi.org/10.1007/978-94-024-1558-2

Daout, S., Jolivet, R., Lasserre, C., Doin, M. P., Barbot, S., Tapponnier, P., et al. (2016). Along-strike variations of the partitioning of convergence across the Haiyuan fault system detected by InSAR. *Geophysical Journal International*, *205*(1), 536–547. https://doi.org/10.1093/GJI/GGW028

Dodds, N. W. (2021). *The mechanical properties of fault zones and earthquake cycle dynamics along the northern margins of the Iranian Plateau*. (Ph.D. Thesis). University of Oxford.

Ferretti, A., Monti-Guarnieri, A., Prati, C., & Rocca, F. (2007). In K. Fletcher (Ed.), *InSAR principles: Guidelines for SAR interferometry processing and interpretation*. ESA Publications, ESTEC.

Grützner, C., Carson, E., Walker, R., Rhodes, E., Mukambayev, A., Mackenzie, D., et al. (2017). Assessing the activity of faults in continental interiors: Palaeoseismic insights from SE Kazakhstan. *Earth and Planetary Science Letters*, *459*, 93–104. https://doi.org/10.1016/j.epsl.2016.11.025

Heimann, S., Kriegerowski, M., Isken, M., Cesca, S., Daout, S., Grigoli, F., et al. (2017). Pyrocko—An open-source seismology toolbox and library [Software]. *GFZ Data Services*. https://doi.org/10.5880/GFZ.2.1.2017.001

NASA JPL. (2013). NASA Shuttle Radar Topography Mission Global 1 arc second [Dataset]. *NASA EOSDIS Land Processes Distributed Active Archive Center*. https://doi.org/10.5067/MEASURES/SRTM/SRTMGL1.003

Ou, Q. (2020). *Crustal strain and seismic hazard of the NE Tibetan Plateau* (Ph.D. Thesis). University of Oxford.

Purcell, V., Reddin, E., Ebmeier, S., González, P. J., Watson, A., Morishita, Y., & Elliott, J. (2022). Nearly three centuries of lava flow subsidence at Timanfaya, Lanzarote. *Geochemistry, Geophysics, Geosystems*, *23*(10), e2022GC010576. https://doi.org/10.1029/2022GC010576

Rosen, P., Hensley, S., Joughin, I., Li, F., Madsen, S., Rodriguez, E., & Goldstein, R. (2000). Synthetic aperture radar interferometry. *Proceedings of the IEEE*, *88*(3), 333–382. https://doi.org/10.1109/5.838084

Stull, R. B. (2017). *Practical meteorology: An algebra-based survey of atmospheric science (Version 1.02b ed.)*. University of British Columbia.

Tsai, C.-H. (2023). *Active tectonics and palaeoseismicity of the northern Tien Shan and Dzhungaria* (Ph.D. Thesis). University of Oxford.

Wright, T. J., Parsons, B. E., & Lu, Z. (2004). Toward mapping surface deformation in three dimensions using InSAR. *Geophysical Research Letters*, *31*(1), L01607. https://doi.org/10.1029/2003GL018827

Yu, C., Li, Z., & Penna, N. T. (2018). Interferometric synthetic aperture radar atmospheric correction using a GPS-based iterative tropospheric decomposition model. *Remote Sensing of Environment*, *204*, 109–121. https://doi.org/10.1016/j.rse.2017.10.038